

**8th Quarterly Progress Report to the
FEDERAL HIGHWAY ADMINISTRATION
(FHWA)**

**On the Project:
THE IMPACT OF WIDE-BASE TIRES ON PAVEMENT
DAMAGE
DTFH61-11-C-00025**

**For period
January 1st to March 31th 2013**

**Submitted by
Illinois Center for Transportation
University of Illinois at Urbana-Champaign**

QUARTERLY PROGRESS REPORT

QUARTER 7

The Impact of Wide-Base Tires on Pavement Damage – A National Study

1. Work performed

During this quarter, the following tasks have been accomplished:

- Issues with the boundaries of the pavement's finite element (FE) model were addressed by performing a detailed mesh sensitivity analysis. This analysis was applied to each combination of thickness considered in this study (Table 1 and Table 2). Appendix A describes the procedure followed and presents the mesh configuration of each pavement structure.
- As part of the development of a realistic tire-inflated model, the material characterization of the tire components was performed (rubber and reinforcement). Rubber components were considered linear viscoelastic, while reinforcements were considered linear elastic. Details regarding the methodology to obtain the input parameters for FE analysis from laboratory testing are given in Appendix B.
- The resilient modulus test result provided by the Minnesota Department of Transportation allows the characterization of granular base as stress-dependent isotropic. In order to fulfill the scope of this study for thin pavement sections, a more advanced material characterization is needed for unbound materials (stress-dependent cross-anisotropic). A database of more than one hundred unbound granular materials was considered for this purpose (Tutumluer, 2008). The resilient modulus test results are based on using vertical and radial pulse loading. Appendix C details the selection procedure of the weak and strong stress-dependent cross-anisotropic granular base for thin pavements.
- Finite element analysis was carried out for the lowest value of load and tire inflation pressure and the smallest thicknesses for both cases: thin and thick pavement structures. Material combinations based on the pavement structure considered for the loading case were also performed. Appendix D provides some results of this analysis.
- Dual tire assembly (DTA) testing for loads less than 18 kips was finished at UC-Davis.

- Initial analysis of the data collected in Ohio and Florida was performed. A filtering procedure was established, and the data files were added to the database. Details regarding these topics are given in Appendix E.
- Coordination with research teams in Florida and UC-Davis has been initiated in order to obtain samples and perform laboratory testing of the materials used during construction of the pavement sections.
- Semi-circular beam (SCB) and Disk Compact Test (DCT) were completed for all four materials from Ohio. Appendix F details the construction process in Ohio.
- Accelerated pavement testing of the sections in the test pit of Florida was completed for both sections (test pit and test track). The collected data have been received by the research team at the University of Illinois. Appendix G summarizes the construction, instrumentation, and testing of the pavement sections if Florida.

Table 1. Thicknesses for thin pavements

Thin Pavement Structure	
	Thicknesses
AC Layer	75 and 125 mm
Base	150 and 600 mm
Subgrade	--

Table 2. Thicknesses for thick pavements

Thick Pavement Structure	
	Thicknesses
Wearing Surface	25 and 62.5 mm
Intermediate Layer	37.5 and 100 mm
Binder Layer	62.5 and 250 mm
Base Granular	150 and 600mm
Base Treated	
Subbase Treated	
Subbase Granular	150 and 600mm
Subgrade	

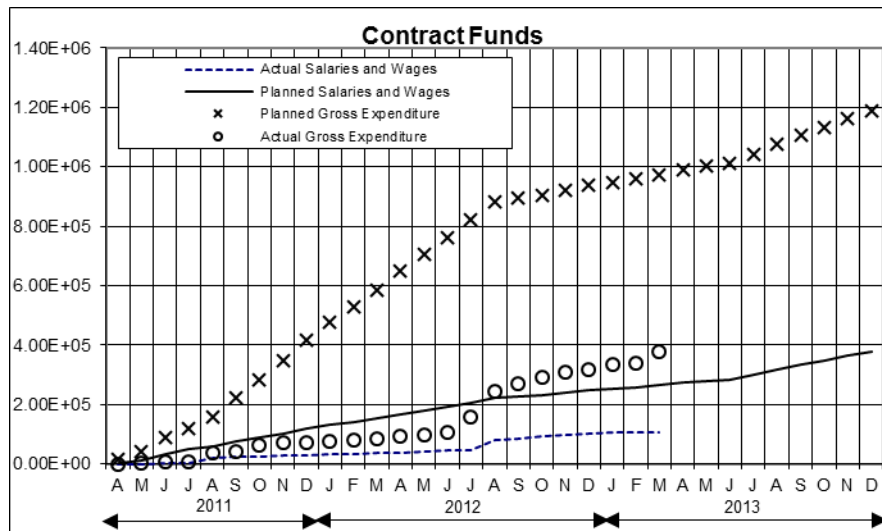
2. Work to be accomplished next quarter

- Laboratory testing of materials collected from Ohio test sections will be finalized. In addition, characterization of materials from Florida and UC-Davis sections will be obtained and testing will be initiated.
- Analysis of the data collected from Florida, UC-Davis, and Ohio will be initialized.
- Mesh sensitivity analysis of the tire-inflated model will be performed.
- FEM analysis of pavement structures will continue.
- Tire reinforcement will be characterized

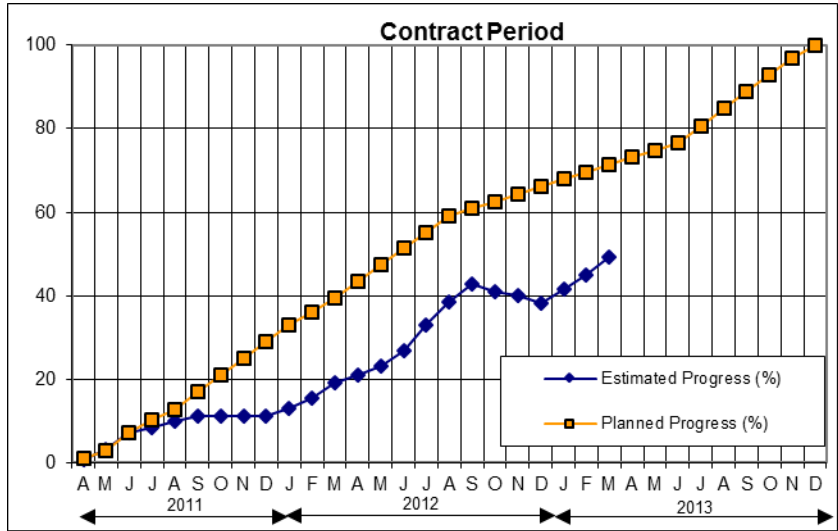
3. Problems encountered

- No problems were encountered in this quarter

4. Current and cumulative expenditures



5. Planned, actual, and cumulative percent of effort



APPENDIX A

MESH SENSITIVITY ANALYSIS

To ensure that pavement responses vanish as the distance from applied load increases, the finite element model must have appropriate dimensions in the three principal orthogonal directions. It has been shown that these dimensions can be unrealistically large if infinite elements at the boundary of the model are not used. The infinite element should be appropriately located so that the dimensions of the model are small enough to minimize the computation time, while fulfilling the half-space assumption. Similarly, the size of the finite elements should be small enough to achieve accurate results; however, to make sure the computational time is reasonable, the finite elements must not be too small.

To address both issues, a parametric study was performed. In that study, the size of the infinite elements was fixed as 500 mm, and the sizes of the other elements in the model varied. The semi-analytical software BISAR was used for validating the finite element results. The optimum mesh was selected as the one with the biggest elements (smallest computation time), bringing pavement responses within a difference of approximately 5% from the ones obtained using BISAR. The following selected pavement responses were compared: maximum longitudinal strain at the bottom of the AC ($\epsilon_{11,ac}$), maximum vertical strain on top of the subgrade ($\epsilon_{22,subg}$), and maximum shear strain in each layer ($\epsilon_{23,ac}$, $\epsilon_{23,base}$, and $\epsilon_{23,subg}$ for asphalt concrete, base, and subgrade, respectively).

To obtain comparable results between BISAR and Abaqus, a 3D model resembling the assumptions of the former was created using the later: axisymmetry, circular load with vertical uniform contact pressure, fully bonded layer interaction, and infinite half-space. Since the computation time of a 3D model is significantly larger than that of a 2D axisymmetric model, the various mesh trials were run using 2D simplification. Once the optimum mesh was found in the 2D axisymmetric model, the corresponding mesh in 3D was created and rechecked with BISAR's results. This procedure was applied for the eight possible combinations of pavement thicknesses considered. Following is a detailed presentation of the described method for the thinnest pavement considered in this study (AC thickness = 75 mm and base thickness = 125 mm). The results of other seven pavement structures are also summarized.

As an initial mesh configuration, the general guidelines provided by Yoo (2007) were adopted: 10 mm or smaller for the elements close to the surface, and between 20 and 50 mm for granular material elements. The length of the infinite elements in the plan view was set at 500 mm. In addition, to have appropriate transition of element size, the *bias* parameter of Abaqus was used. This value represents the ratio between the dimension of the first and the last element along an edge.

The mesh configuration in the plain view is dictated by the tire footprint and its transition to the boundary of the model; the element close to the loaded area is relatively small, and it gradually increases as it approaches the boundary. Figure 1 presents the dimensions defining the model in the plan view. The total length and width of the model are L and B , respectively. In addition, X is the length along which the tire is moving, and b is the width of the tire footprint. A transition from the small elements around the loading area to the infinite elements in the model boundary is also shown and is defined by $L1$, $L2$, $B1$, and $B2$. Finally, D is the model's depth.

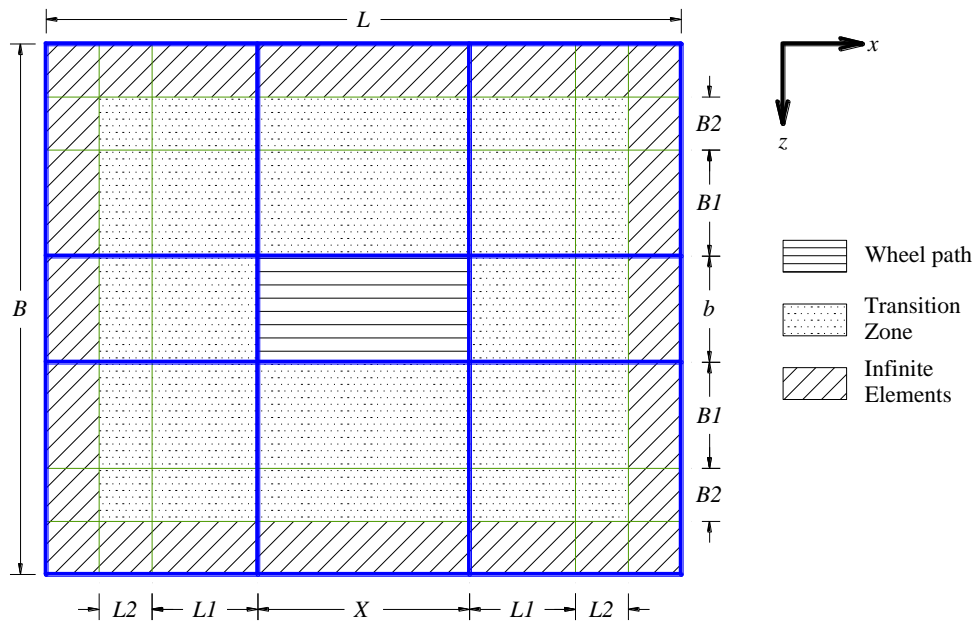


Figure 1. Typical dimension in plan view

In the axisymmetric model, the following element types were used: CAX4 (continuum, axisymmetric, 4-node bilinear) in the AC and base layer; CAX4R (continuum, axisymmetric, 4-node bilinear with reduced integration) in the subgrade, and CINAX4 (4-node axisymmetric

infinite element) at the boundaries. After iterations, it was found that the optimum thicknesses of the elements in the axisymmetric model are 6.25 mm for the AC, between 9.5 and 16.1 mm for the base, and 16.2 mm for the element on top of the subgrade. The optimum mesh of the axisymmetric model was recreated in 3D, and results were compared to those from BISAR. In this case, the elements used were C3D8 (continuum, three dimensional, 8-node) for the AC and base, C3D8R (continuum, three-dimensional, 8-node with reduced integration) for the subgrade and CIN3D8 (three-dimensional, 8-node, infinite element) for the boundary. Figure 2 shows the axisymmetric and 3D models in Abaqus.

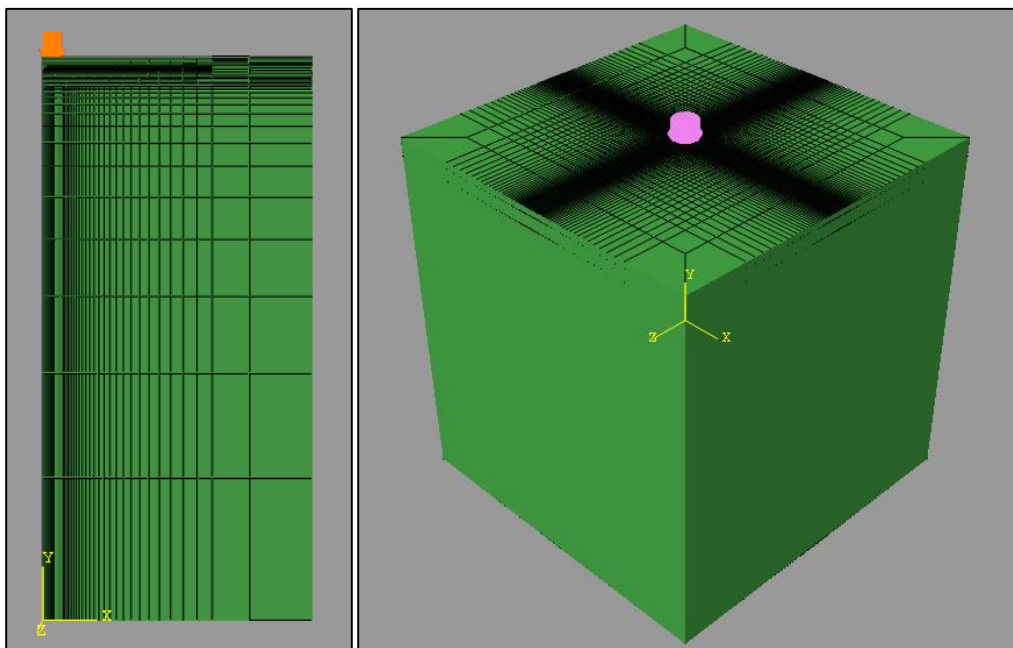


Figure 2. Axisymmetric and 3D FEM model of the optimum mesh configuration

After comparing the results between the 3D model in Abaqus and BISAR, the resulting difference was always found to be equal or less than 5%. The same process was repeated for each of the other seven pavement structures. A summary of the results for the thin and thick pavement structures is presented in Table 3 and Table 4, while Table 5 and Table 6 present the comparison between BISAR and the 3D model in Abaqus. The 3D model used to determine the optimum mesh does not take into account the moving load. When moving load is considered, the total length of the model is the length of the wheel path, the transmission length, and the length of the infinite elements.

Table 3. Mesh details for thin pavement structures

Thin Pavements		Model			
		AC=75 mm, Base=150 mm	AC=75 mm, Base=600 mm	AC=125 mm, Base=150 mm	AC=125 mm, Base=600 mm
Dimensions (mm)	<i>L</i>	4300	5800	4800	5300
	<i>B</i>	4300	5800	4800	5300
	<i>D</i>	4500	4500	4500	4500
	<i>L1 = B1</i>	1200	1950	1450	1700
	<i>L2 = B2</i>	300	300	300	300
AC	No. Elem.	12	12	15	15
	Bias	1.0	1.0	1.2	1.2
Base	No. Elem.	12	25	12	25
	Bias	1.7	1.3	1.7	1.0
Subgrade	No. Elem.	15	15	15	15
	Bias	70.0	30.0	50.0	30.0
<i>L1 = B1</i>	No. Elem.	25	30	30	25
	Bias	10.0	20.0	10.0	15.0
<i>L2 = B2</i>	No. Elem.	1	1	1	1
	Bias	1.0	1.0	1.0	1.0

Table 4. Mesh details for thick pavement structure

Thick Pavements		Model			
		AC=125 mm, Base=150 mm	AC=125 mm, Base=600 mm	AC=412 mm Base=150 mm	AC=412 mm, B=600 mm
Dimensions (mm)	<i>L</i>	4300	5300	7400	7900
	<i>B</i>	4300	5300	7400	7900
	<i>D</i>	4500	4500	4500	4500
	<i>L1 = B1</i>	1250	1700	2750	3000
	<i>L2 = B2</i>	250	300	300	300
Wearing Surface	No. Elem.	4	4	5	5
	Bias	1.0	1.1	1.2	1.2
Intermediate Layer	No. Elem.	5.0	5.0	6.0	6.0
	Bias	1.2	1.0	1.4	1.4
Binder Layer	No. Elem.	7.0	7.0	12.0	9.0
	Bias	1.15	1.20	1.00	1.00
Base	No. Elem.	12	25	7	22
	Bias	1.5	1.0	1.0	1.0
Subgrade	No. Elem.	15	15	15	15
	Bias	75.0	30.0	30.0	25.0

$L1 = B1$	No. Elem.	15	20	30	30
	Bias	10.0	15.0	20.0	20.0
$L2 = B2$	No. Elem.	1	1	1	1
	Bias	1.0	1.0	1.0	1.0

Table 5. Comparison between Abaqus and BISAR for thin pavements

	AC=75 mm, Base=150 mm			AC=75 mm, B=600 mm.			AC=125 mm, Base=150 mm			AC=125 mm, Base=600 mm		
	Abaq.	BIS.	Dif. (%)	Abaq.	BIS.	Dif. (%)	Abaq.	BIS.	Dif. (%)	Abaq.	BIS.	Dif. (%)
$\epsilon_{11,ac}$	126.5	133.8	5.5	105.4	111.3	5.3	63.9	67.2	4.9	56.6	59.5	4.9
$\epsilon_{22,subg}$	817.9	836.8	2.3	354.6	364.4	2.7	341.0	348.9	2.3	206.5	212.6	2.9
$\epsilon_{23,ac}$	27.0	27.4	1.4	25.5	26.1	2.3	17.0	17.0	0.2	16.4	16.5	0.7
$\epsilon_{23,base}$	193.0	190.4	1.4	179.1	170.7	4.9	68.4	67.9	0.8	75.2	73.0	3.0
$\epsilon_{23,subg}$	269.9	276.6	2.4	128.7	135.1	4.8	101.6	103.9	2.2	70.6	75.8	6.9

Table 6. Comparison between Abaqus and BISAR for thick pavements

	AC=125 mm, Base=150 mm			AC=412 mm, Base=600 mm			AC=125 mm, B=150 mm			AC=412 mm, Base=600 mm		
	Abaq.	BIS.	Dif. (%)	Abaq.	BIS.	Dif. (%)	Abaq.	BIS.	Dif. (%)	Abaq.	BIS.	Dif. (%)
$\epsilon_{11,ac}$	65.6	68.1	3.7	61.1	63.8	4.2	9.9	9.4	5.2	9.1	9.7	6.3
$\epsilon_{22,subg}$	300.0	295.5	1.5	157.4	159.7	1.4	36.0	36.1	0.3	27.9	27.8	0.3
$\epsilon_{23,ac}$	19.4	19.2	1.0	19.8	19.4	1.8	7.3	7.6	4.0	7.6	7.3	4.2
$\epsilon_{23,base}$	73.3	70.0	4.7	74.9	74.7	0.3	6.8	6.6	3.3	7.9	8.0	1.3
$\epsilon_{23,subg}$	83.2	88.2	5.7	53.7	56.6	5.1	8.5	8.1	5.0	7.8	8.2	4.8

APPENDIX B

MATERIAL PROPERTIES OF TIRE COMPONENTS

Appropriate material characterization is a key component of any finite element model. Two main types of materials compose a tire: rubber and steel reinforcement. It has to be noted that truck tires experience large deformations when subjected to truck load, so hyperelastic characterization is more appropriate than linear elastic. Furthermore, the response of rubber varies with rate of loading and temperature, creating the need to consider it a viscoelastic material. For steel reinforcement, linear elastic behavior has been shown to be suitable.

RUBBER COMPONENTS

Selected rubber components of each tire were characterized. For WBT, five rubber constituents were tested: tread, sub-tread, shoulder, sidewall, and bead filler. The components tested for the DTA were tread, shoulder, sidewall, and bead filler.

The viscoelastic characterization of rubber was performed following ASTM E1640. Four values of frequency (0.01, 0.1, 1.0, and 10.0) and seven values of temperature (−58.0, −13.0, 32.0, 77.0, 122.0, 167.0, and 212.0 °F) were used to test in tension a rubber sample using a dynamic mechanical analyzer. The test provides the storage (E') and loss (E'') moduli, as well as the phase angle (δ). Based on the linear viscoelastic theory, it is known that the complex modulus (E^*) is the following:

$$E^*(\omega) = E'(\omega) + iE''(\omega)$$

Using the generalized Maxwell Model, it is possible to derive an expression as a function of time for the relaxation modulus $E(t)$ (Prony series):

$$E(t) = E_e + \sum_{i=1}^m E_i e^{-t/\tau_i}$$

where: E_e = equilibrium modulus;

E_i = relaxation strength (Prony series terms);

τ_i = relaxation times; and

m = number of Maxwell elements.

The following can also be proved:

$$E'(\omega) = E_e + \sum_{i=1}^m \frac{\omega^2 \tau_i^2 E_i}{\omega^2 \tau_i^2 + 1}$$

$$E'(\omega) = \sum_{i=1}^m \frac{\omega \tau_i E_i}{\omega^2 \tau_i^2 + 1}$$

Using the $E'(\omega)$ from the test results and setting τ_i , it is possible to formulate an over-determined system of linear algebraic equation that can be solved using the least-squares method. The solution of the system of equation is the Prony series terms E_i . It is important to note that Abaqus uses the Prony series expansion to consider linear viscoelastic materials. The least-squares method is applied on the master curve of E' . As a consequence, the raw data from the test must be shifted. The shift factor relates the frequency (ω) of the test and the reduced frequency (ξ):

$$a_T = \frac{\xi}{\omega}$$

Furthermore, Abaqus considers the temperature effect using the Williams-Landel-Ferry (WLF) equation:

$$\log a_T = -\frac{C_1(T - T_o)}{C_2 + (T - T_o)}$$

where: T = testing temperature;

T_o = reference temperature (77°F); and

C_1, C_2 = regression coefficients.

In summary, the procedure to determine the parameters required by Abaqus to consider linear viscoelasticity is as follows:

- Using $E'(\omega)$ from the dynamic analyzer, the master curve was built (Figure 3 and Figure 4). Each figure shows not only the master curve but also the storage modulus at each temperature after shifting. The continuous line corresponds to the calculated master curve after the Prony series terms were computed. The variation of the shift factor with temperature for each material is presented in Figure 5 and Figure 6. The WLF regression coefficients are also reported.
- Using the Prony series terms, the relaxation modulus $E(t)$ can be calculated. The variation of $E(t)$ with time for each tested rubber component is shown in Figure 7 and Figure 8.

Storage Modulus WBT Rubber

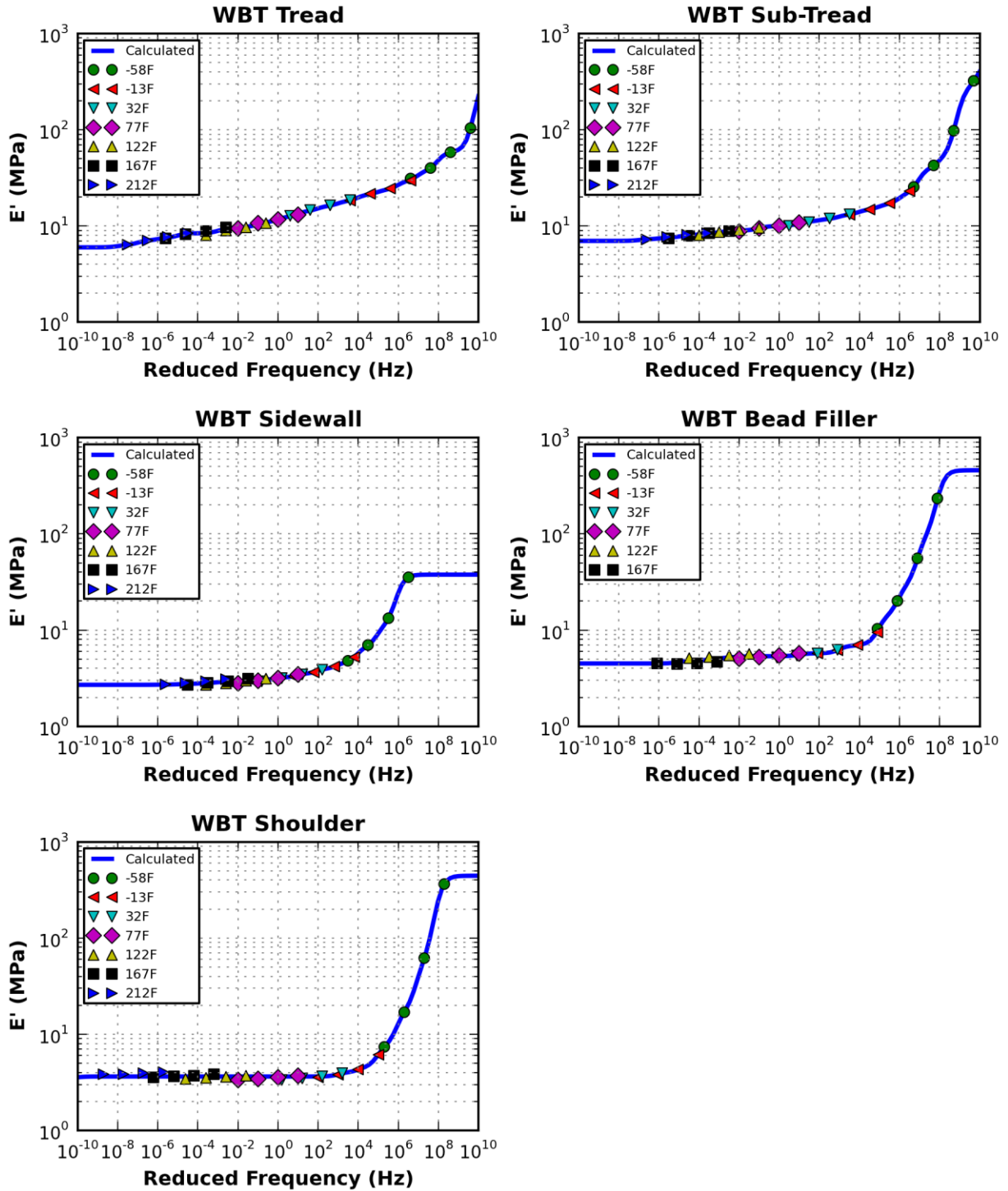


Figure 3. Master curve of storage modulus of rubber components for WBT

Storage Modulus DTA Rubber

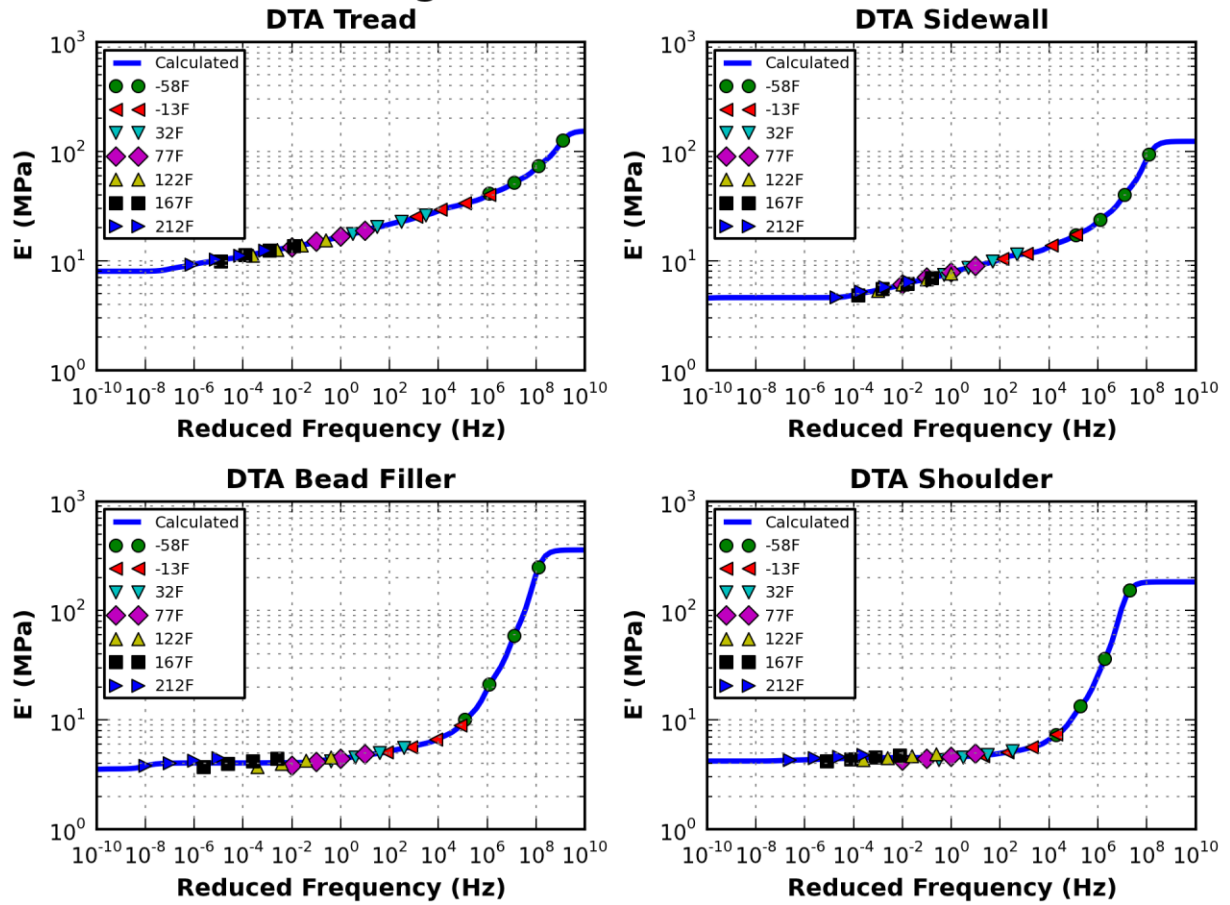


Figure 4. Master curve of storage modulus of rubber components for DTA

Shift Factor WBT Rubber

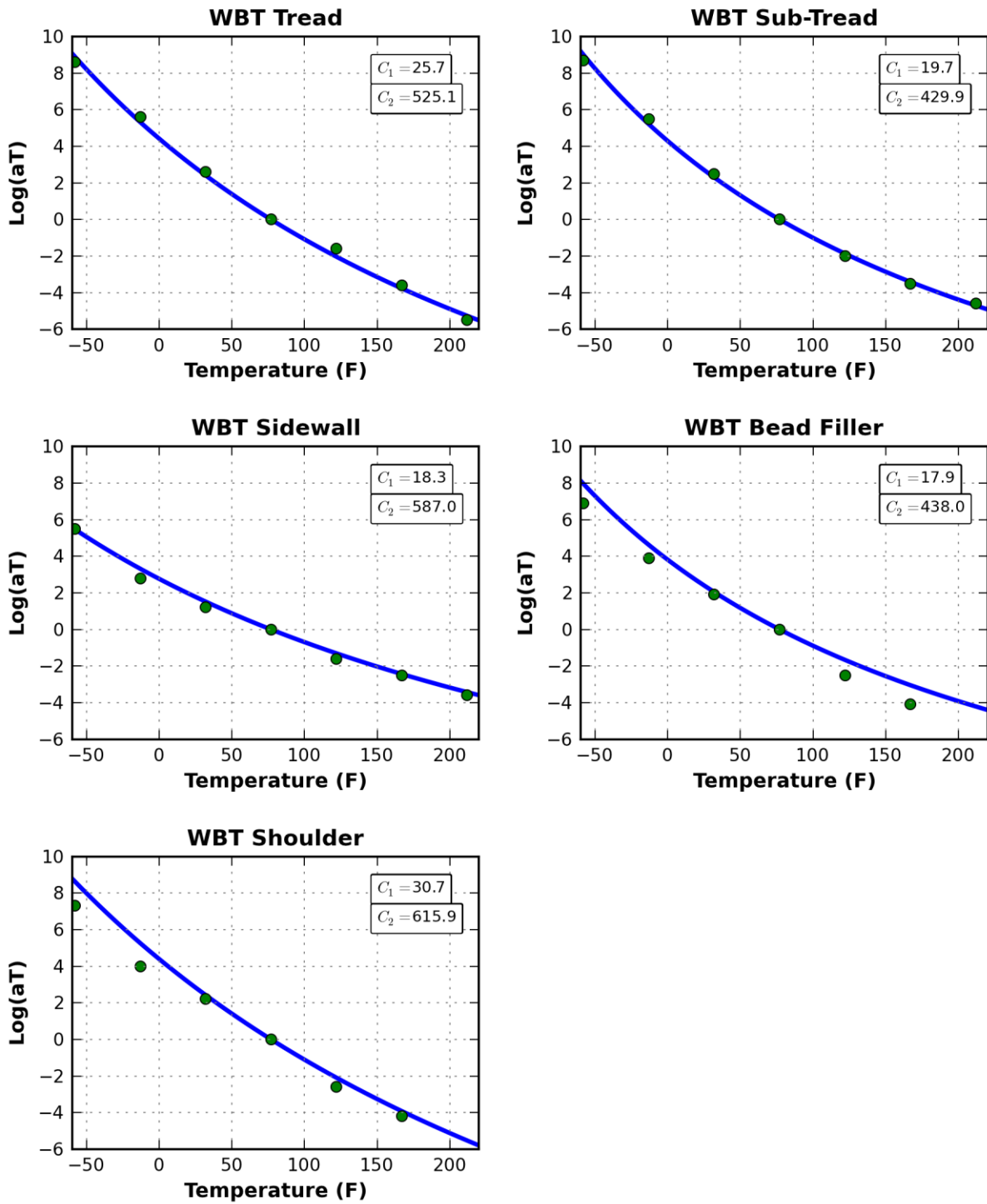


Figure 5. Variation of shift factor with temperature and WLF coefficients for WBT

Shift Factor DTA Rubber

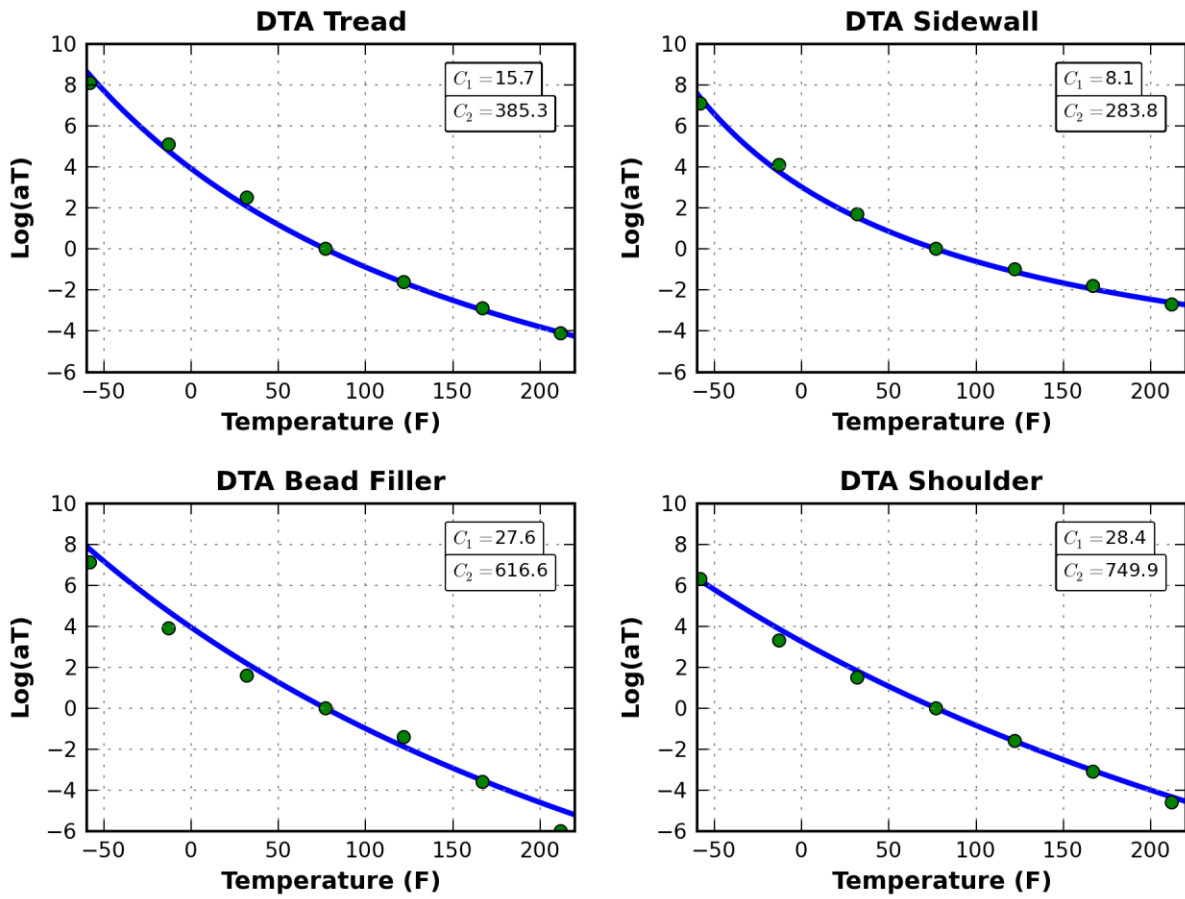


Figure 6. Variation of shift factor with temperature and WLF coefficients for DTA

Relaxation Modulus WBT Rubber

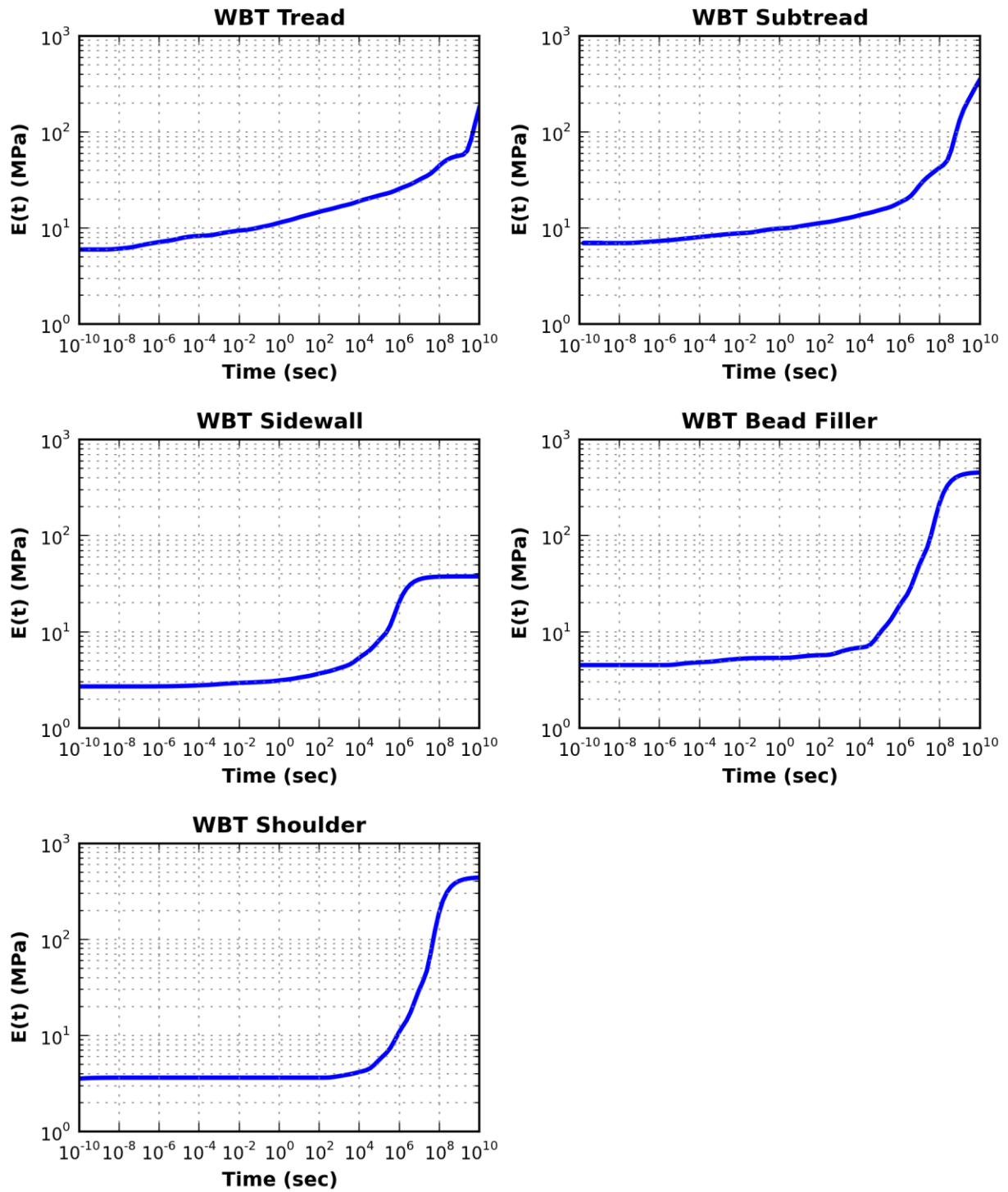


Figure 7. Relaxation modulus for rubber components of WBT

Relaxation Modulus DTA Rubber

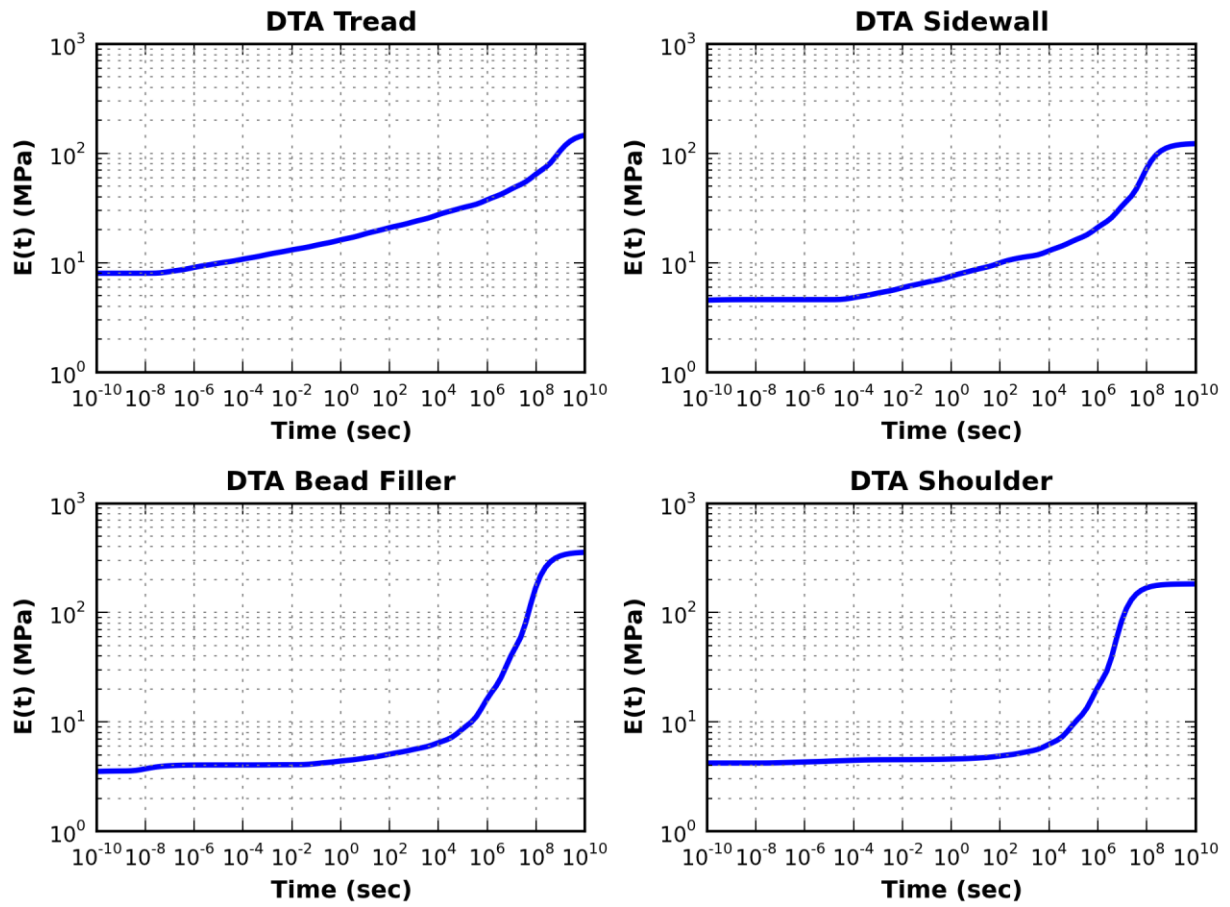


Figure 8. Relaxation modulus of rubber components of DTA

APPENDIX C
GRANULAR MATERIALS SELECTION

To select appropriate strong and weak base materials, a database of 114 materials with appropriate nonlinear cross-anisotropic laboratory characterization was considered (Tutumlu, 2008). The laboratory test applies pulse load in the vertical and radial directions. Hence, cross-anisotropic characterization is possible. A description of the procedure used to determine weak and strong base materials utilized in the FEM analysis is presented. As part of the database, k -values based on the Uzan model are reported. The Uzan model is as follows:

$$M_{rv} = k_1 \left(\frac{\theta}{p_o} \right)^{k_2} \left(\frac{\sigma_d}{p_o} \right)^{k_3}$$

where: M_{rv} = resilient modulus in the vertical direction;

k_1, k_2, k_3 = regression coefficients;

$\theta = \sigma_1 + \sigma_2 + \sigma_3$ = bulk stresses;

σ_d = deviator stress; and

p_o = unit reference pressure.

It is known that the resilient modulus of granular materials depends on the stress level. To select appropriate weak and strong base materials, two stress levels (Table 7) were defined based on the field condition of base materials (Xiao et al., 2011).

Table 7. Stress level for low and high resilient moduli

	Low		High	
	kPa	Psi	kPa	psi
σ_3	34.9	5.0	104.8	15.0
σ_d	104.8	15.0	209.5	30.0
σ_1	139.7	20.0	314.3	45.0
σ_2	34.9	5.0	104.8	15.0
θ	209.5	30.0	523.9	75.0

Using the aforementioned stress levels and the k -values from the database, the resilient modulus for each material was calculated. The obtained resilient moduli for both stress states are

presented in Figure 9. Assuming a normal distribution, the weak base material was selected as the one corresponding to the average, minus two standard deviations ($\mu - 2\sigma = 9.8$ ksi) of the set of the resilient modulus corresponding to low stress level. Similarly, the strong base material corresponded to the closer value of the vertical resilient modulus of $\mu + 2\sigma = 47.3$ ksi. After the materials were selected, laboratory data from the database were used to determine the k -values utilizing the ME-PDG model.

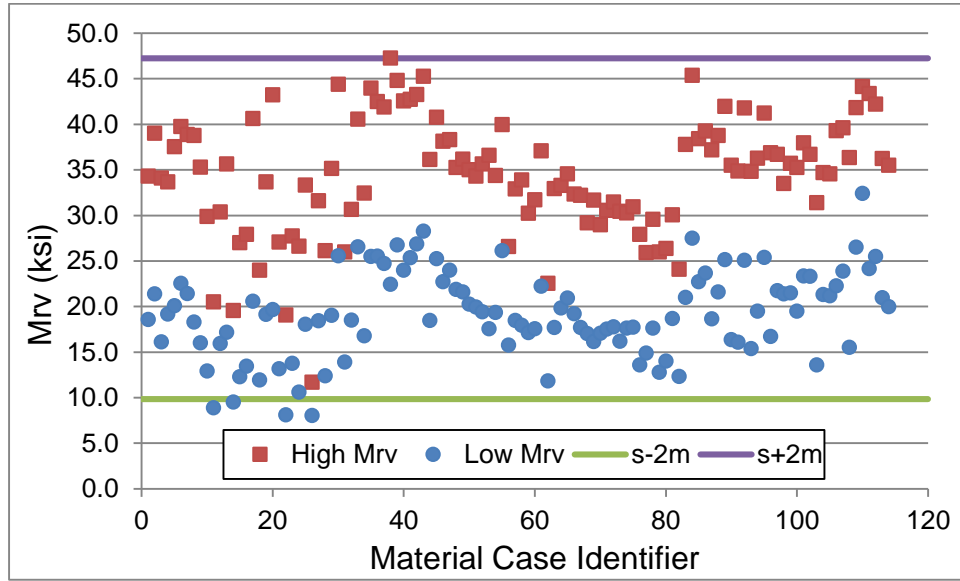


Figure 9. Resilient modulus for low and high stress levels

It is important to note that pulse loading was not applied in the shear direction during laboratory testing; hence, a simplified procedure proposed by Tutumluer and Thompson (1998) was utilized to determine the k -values in the shear direction. The procedure is summarized as follows:

- In the case of cross-anisotropy, the Uzan model becomes:

$$M_{rv} = k_1 \left(\frac{\theta}{p_o} \right)^{k_2} \left(\frac{\sigma_d}{p_o} \right)^{k_3}$$

$$M_{rh} = k_4 \left(\frac{\theta}{p_o} \right)^{k_5} \left(\frac{\sigma_d}{p_o} \right)^{k_6}$$

$$M_{rs} = k_7 \left(\frac{\theta}{p_o} \right)^{k_8} \left(\frac{\sigma_d}{p_o} \right)^{k_9}$$

Note that the database provides values for k_1 through k_6 .

- Using a simplified method proposed by Tutumluer and Thompson (1998), the shear k -values for the shear direction are calculated:

$$k_7 = -90.92 + 0.27k_1 + 305.34k_2 + 158.22k_3 \text{ (psi)}$$

$$k_8 = 0.2 + k_2$$

$$k_9 = -0.2 + k_3$$

- Utilizing k_7 , k_8 , and k_9 and the stress levels of the vertical resilient modulus, the shear resilient modulus data can be computed.
- Regression parameters of the ME-PDG model are obtained from the resilient moduli in the vertical, horizontal, and shear directions. The ME-PDG version of the nonlinear cross-anisotropic model is the following:

$$M_{rv} = k_1 p_a \left(\frac{\theta}{p_a} \right)^{k_2} \left(\frac{\tau_{oct}}{p_a} + 1 \right)^{k_3}$$

$$M_{rh} = k_4 p_a \left(\frac{\theta}{p_a} \right)^{k_5} \left(\frac{\tau_{oct}}{p_a} + 1 \right)^{k_6}$$

$$M_{rs} = k_7 p_a \left(\frac{\theta}{p_a} \right)^{k_8} \left(\frac{\tau_{oct}}{p_a} + 1 \right)^{k_9}$$

The regression parameters for the selected materials are summarized in Table 8. In addition, Table 9 details the calculation of the resilient modulus for both stress levels and materials, while Figure 10 compares the measured and calculated resilient moduli of the selected materials. The resilient modulus in the vertical direction for the strong material at high stress level is 297.7 MPa (42.7 ksi) and for the weak material at low stress level is 69.4 MPa (9.9 ksi). Recall that for thick pavements the resilient modulus for weak and strong granular base was set as 140.0 MPa (20.0 ksi) and 415.0 MPa (60.0 ksi), respectively.

Table 8. Regression parameters of the ME-PDG model for weak and strong granular materials

Direction	Weak			Strong		
Vertical	$k_1=453.3$	$k_2=0.8858$	$k_3=-0.5713$	$k_1=869.6$	$k_2=0.9785$	$k_3=-0.5673$
Horizontal	$k_4=282.4$	$k_5=0.6701$	$k_6=-1.1341$	$k_4=596.6$	$k_5=1.1419$	$k_6=-1.3464$
Shear	$k_7=310.3$	$k_8=1.0297$	$k_9=-1.1036$	$k_7=389.1$	$k_8=0.9083$	$k_9=-0.2409$

Table 9. Summary results of resilient moduli in the vertical, horizontal, and shear directions for both materials at two stress levels

	WEAK				STRONG			
	MPa		psi		MPa		psi	
	Low	High	Low	High	Low	High	Low	High
σ_3	0.0349	0.1048	5.0	15.0	0.0349	0.1048	5.0	15.0
σ_d	0.1048	0.2095	15.0	30.0	0.1048	0.2095	15.0	30.0
σ_1	0.1397	0.3143	20.0	45.0	0.1397	0.3143	20.0	45.0
σ_2	0.0349	0.1048	5.0	15.0	0.0349	0.1048	5.0	15.0
θ	0.2095	0.5239	30.0	75.0	0.2095	0.5239	30.0	75.0
p_a	0.1000	0.1000	14.3	14.3	0.1000	0.1000	14.3	14.3
t_{oct}	0.0494	0.0988	7.1	14.1	0.0494	0.0988	7.1	14.1
M_{rv}	69.41	132.75	9937.2	19006.3	142.8	297.7	20447.4	42624.8
M_{rh}	29.41	39.30	4210.0	5626.9	80.88	156.75	11579.9	22442.3
M_{rs}	42.68	80.00	6110.7	11453.4	69.16	148.40	9901.9	21246.4
M_{rh}/M_{rv}	0.42	0.30	0.42	0.30	0.57	0.53	0.57	0.53
M_{rs}/M_{rv}	0.61	0.60	0.61	0.60	0.48	0.50	0.48	0.50

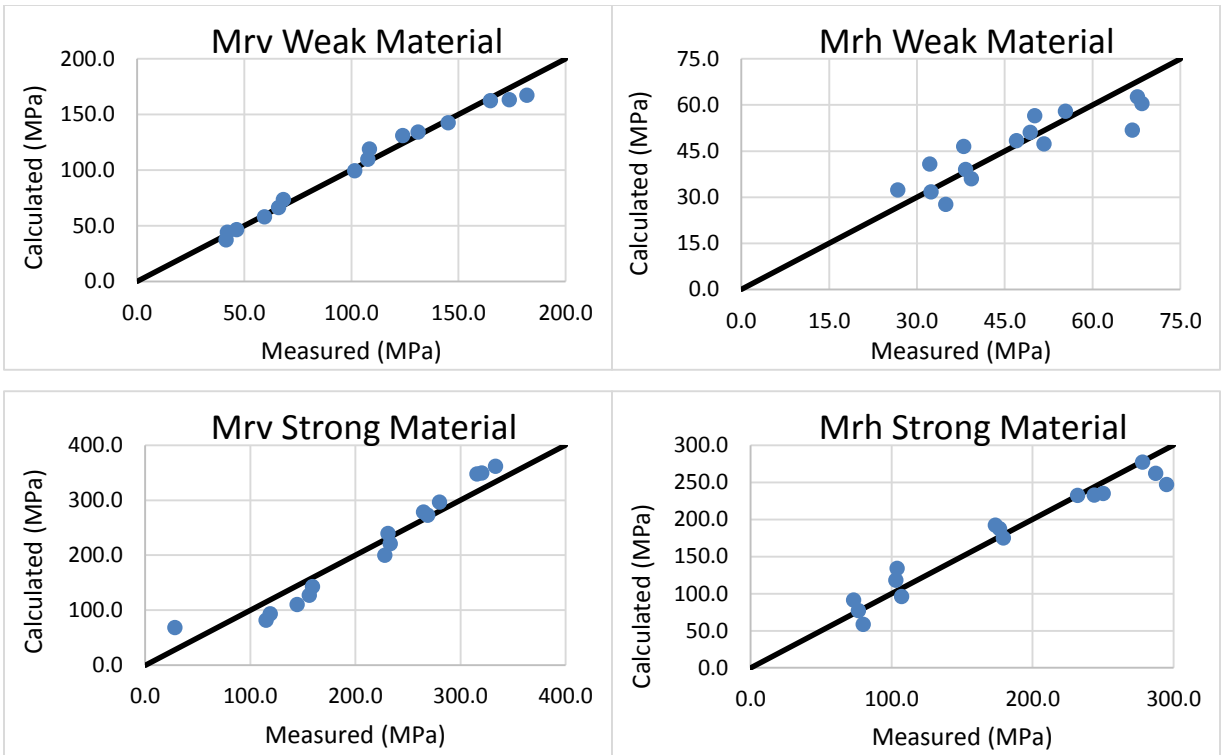


Figure 10. Comparison between measured and calculated resilient moduli

APPENDIX D

SAMPLE OF FEM RESULTS

Figure 11 and Figure 12 present pavement responses for the two extreme loads (WBT) applied to an AC and base thicknesses of 75 mm and 150 mm, respectively.

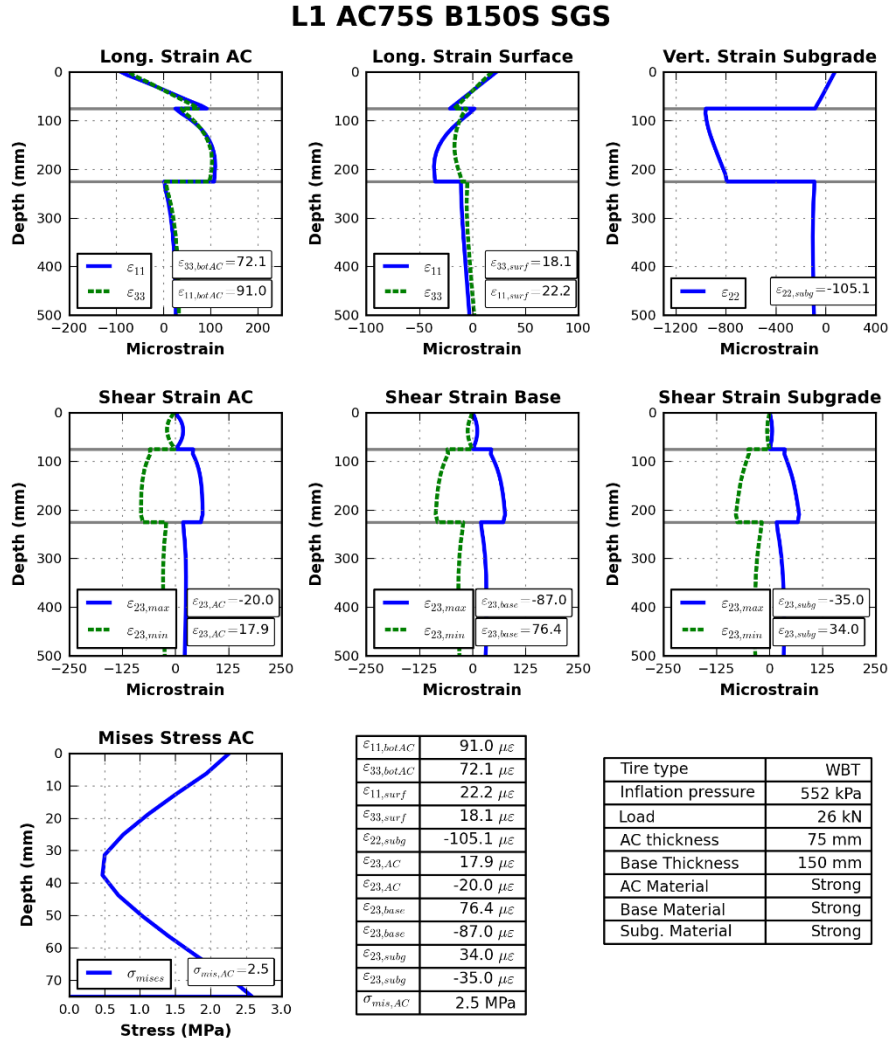


Figure 11. Pavement responses for thinnest pavement, low load, low inflation pressure, WBT, and strong materials

L4 AC75S B150S SGS

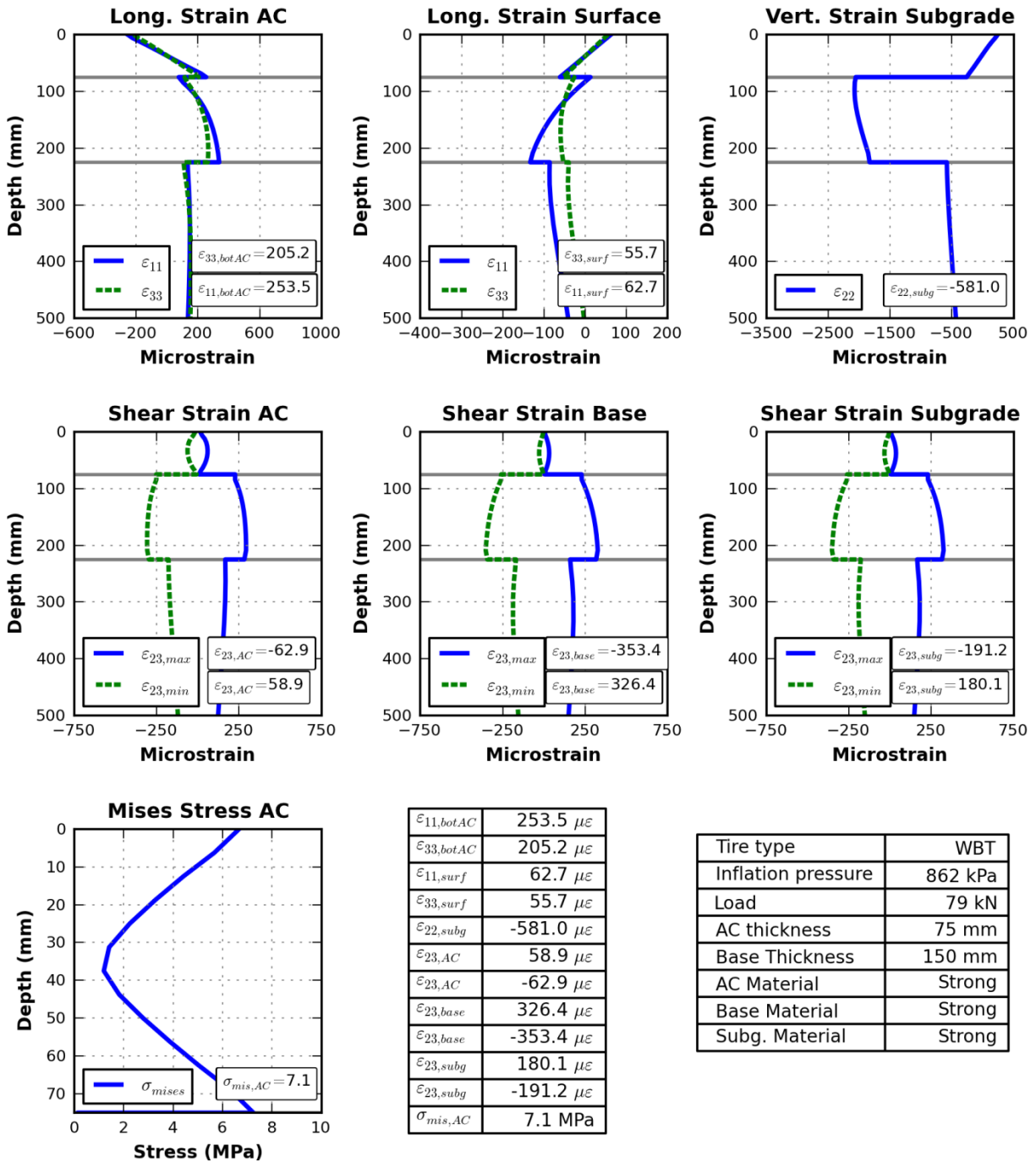


Figure 12. Pavement responses for thinnest pavement, high load, high tire inflation pressure, WBT, and strong materials

APPENDIX E

INVENTORY AND DATA MANAGEMENT

Prior to and during the project, a useful amount of data were collected by the participating groups. Managing and organizing these data are crucial steps. This appendix summarizes the efforts to organize the data. There are five major existing sources of data available to this project; some of them are continuously being updated. These sources are the University of Illinois (UIUC-ATREL), Virginia Tech Smart Road, Florida DOT, UC-Davis, and Ohio SPS-8. The new data come from Florida DOT, UC-Davis, and Ohio SPS-8.

The inventory, in general, includes pavement test section responses collected from various sensor readings and measurements. Each data source will be concisely described in the following sections.

Steps followed in the data management are as follows: receiving the data, understanding the overall and technical aspects of the data, organizing the data, filtering pavement response raw data, and updating the interface for accessing the data or data inquiry. As one of the data management steps, a user-friendly interface was designed to allow easy access of the data and/or inquiry.

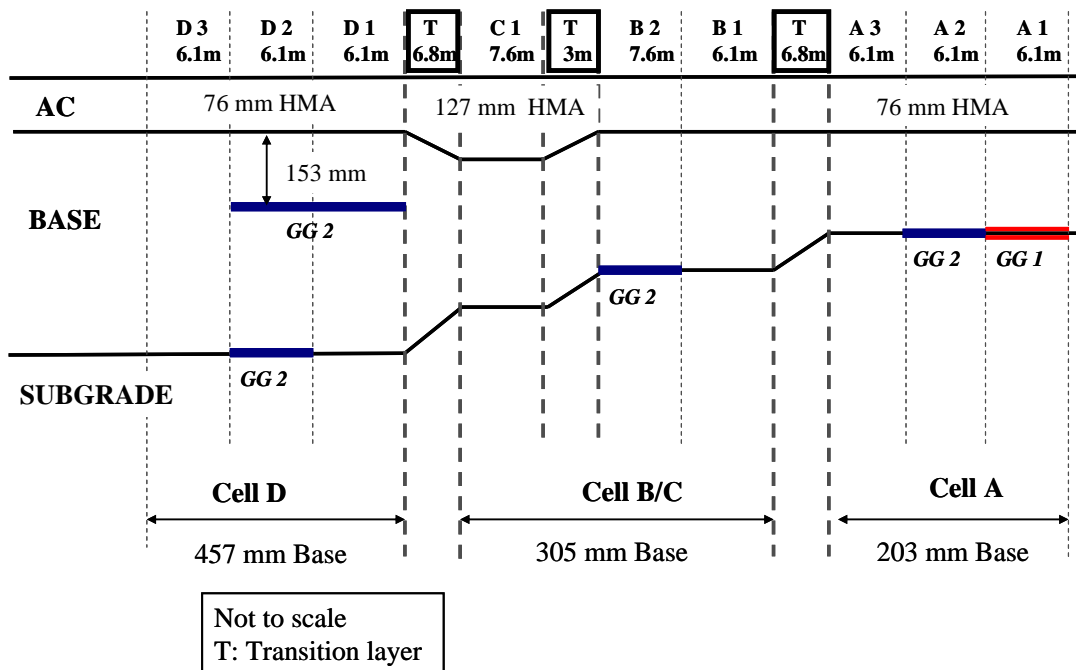
EXISTING DATA

As of today, data are available from UIUC-ATREL, Virginia Tech Smart Road, UC-Davis (contact stresses and profiles), Florida DOT (surface strain and rutting), and Ohio SPS-8 (SHRP Test Road Hot Weather Shear Experiment).

UIUC-ATREL

To quantify the effectiveness of geogrid-reinforced flexible pavements, full-scale accelerated pavement testing was conducted. Nine flexible pavement sections were constructed and tested at the University of Illinois Advanced Transportation Research and Engineering Laboratory (ATREL). The nine sections were divided into three categories based on the total thickness of the pavement system structure (Al-Qadi et al., 2008); see Figure 13.

The variables considered in this full-scale testing study were (1) tire type (one dual and two wide-base tire configurations); (2) type and stiffness of geogrid reinforcement; (3) pavement layer thicknesses; and (4) location of the geogrid within the aggregate base. The sections were heavily instrumented with load-associated instrumentation such as pressure cells, linear variable displacement transducers (LVDTs), and strain gauges. Environmental conditions were also monitored throughout the test using thermocouples, time-domain reflectometry (TDR) probes, and piezometers. The subgrade California bearing ratio (CBR) was maintained below 4% throughout all tested sections. The test sections were loaded utilizing the University of Illinois Advanced Transportation Loading Assembly (ATLAS). Response testing was conducted by applying five load levels at two trafficking speeds and three tire inflation pressures. Then, a 44.5-kN loading was applied at 8 km/h until the pavement sections failed (25 mm or more ruts in the wheel paths).



GG1: Tensar BX1100 and GG2: Tensar BX1200 geogrids

Figure 13. Cross-sections of the full-scale flexible pavement test sections

UC-Davis

UC-Davis data include results from accelerated pavement tests using the Caltrans Heavy Vehicle Simulator (HVS) for two overlay strategies tested at the University of California, Berkeley

Pavement Research Center. These strategies are dense-graded asphalt concrete (DGAC) and asphalt-rubber hot mix gap-graded (ARHM-GG) overlays (Harvey and Popescu, 2000). The data are from tests conducted at elevated temperatures to evaluate the rutting performance of the two overlay strategies. The tests also investigated the effects of tire type, temperature, and thickness of the ARHM-GG overlay. Table 10 summarizes the matrix of primary experiment variables and associated test numbers, and the additional tests.

Table 10. Matrix of HVS test experiment variables and test numbers (after Harvey and Popescu, 2000)

	ARHM-GG Overlay*		DGAC Overlay**	
	50°C at 50 mm depth		50°C at 50 mm depth	40°C at 50 mm depth
Dual Radial	38 mm thick*	62 mm thick*		
Dual Bias-Ply	510RF	509RF	506RF	
Wide-Base Single			505RF	
Aircraft	511RF	508RF	507RF	512RF
			513RF	

* design thickness

** design thicknesses of 62 and 75 mm; actual thicknesses varied

Florida DOT

The primary objective of the research was to assess the impact on pavement performance of different tire designs: (1) a conventional dual tire configuration; (2) two types of new-generation wide-base (NGWB) tires; and (3) a first-generation wide-base tire (Greene et al., 2010). The four tire systems are as follows:

1. Goodyear Unisteel G149 RSA, 11R22.5 (Dual Tire)
2. Goodyear G286 A SS, 425/65R22.5 (Super Single)
3. Michelin X One XDA-HT Plus, 445/50R22.5 (NGWB 445-mm)
4. Michelin X One XDA-HT Plus, 455/55R22.5 (NGWB 455-mm)

Several aspects of the tire and pavement interaction were investigated. As part of the accelerated pavement testing (APT) portion of this study, six test lanes (numbered 2 through 7) were constructed consisting of both open- and dense-graded asphalt surface textures, complying with all standard Florida DOT construction, materials, and in-place (as constructed) methods and specifications. Each lane was trafficked until a rut depth of approximately 0.50 in (12.5 mm) was measured. Lane 1, which was constructed similarly to Lanes 2 through 4, was used to measure

surface strain caused by each tire. The dense-graded pavement structure and tire interaction was modeled using FE analysis to determine the theoretical pavement response to the different tires.

Ohio SPS-8

The Federal Highway Administration (FHWA) conducted controlled loading tests on the U.S. Route 23 test road in hot weather conditions in Ohio (Xue and Weaver, 2011). The testing was done using four tire types, in both dual and wide-base configurations, that were fitted on a single-unit two-axle truck, maintaining a constant gross vehicle weight. Two pavement sections, one 8-in (204 mm) and one 4 in (102 mm) thick were instrumented with strain gage rosettes oriented vertically to measure strain traces induced from the passing wheel loads at three different speeds and tire inflation pressures. Pavement temperature was monitored with depth during testing as well as wheel track offset distance from the strain sensors.

INTERFACE DESIGN

A user-friendly interface was designed to allow access to data. Figure 14 shows a snapshot of the main menu of the interface. It includes the aforementioned five major databases. By selecting each database, the user can access the data as well as all reports, papers, images, and other documents related to that data. Figure 15 presents a snapshot from the UIUC-ATREL database as an example. The data are stored in different formats according to the size of data and systems of acquisition, as well for as user convenience.

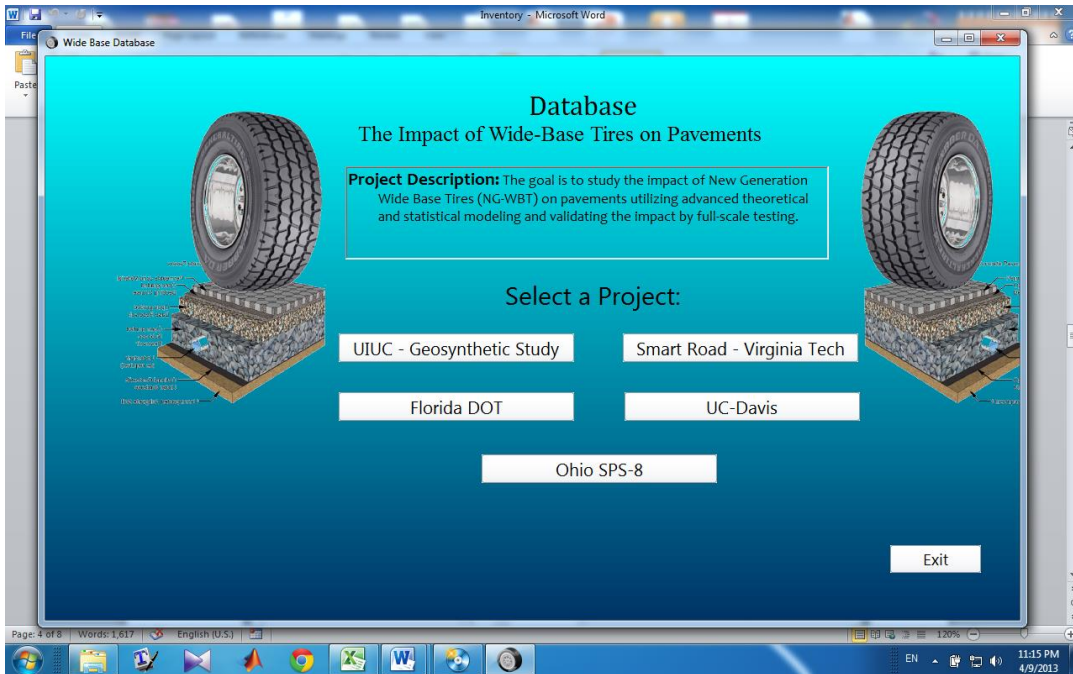


Figure 14. Snapshot from main menu of the interface.

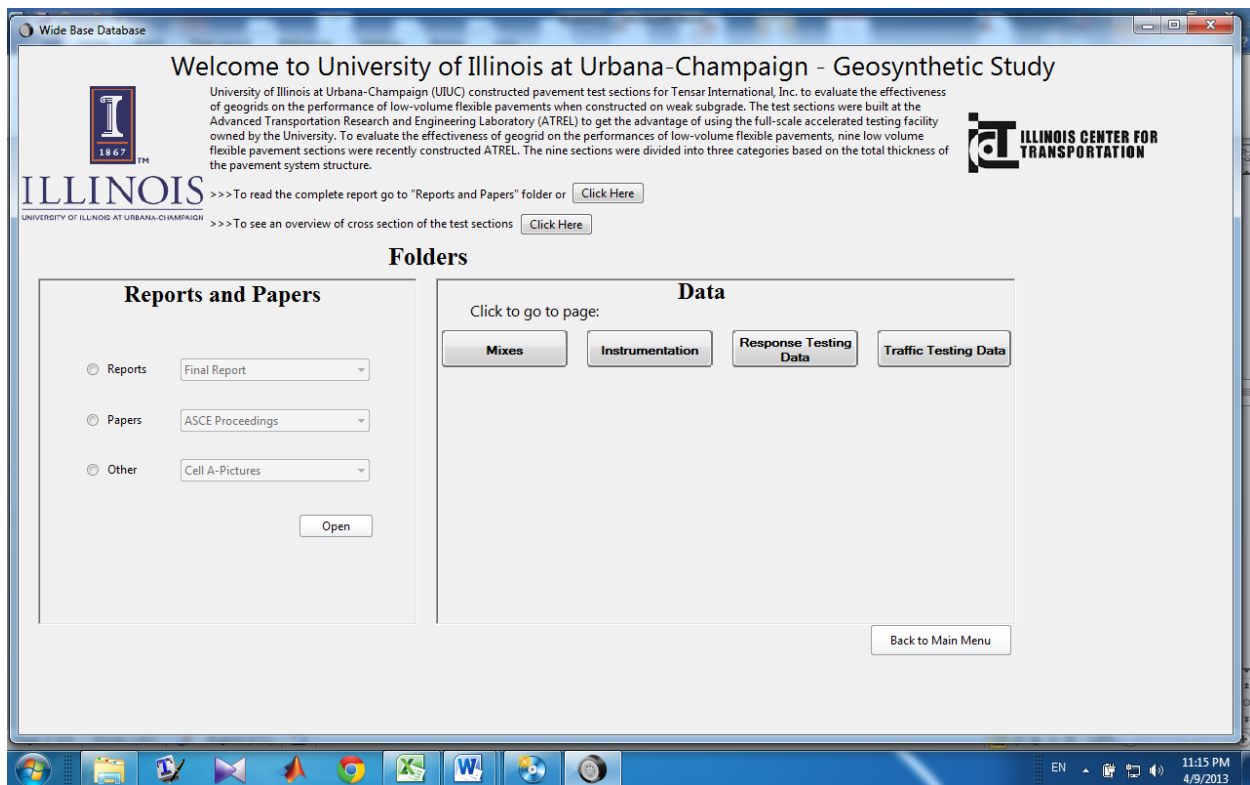


Figure 15. Snapshot from UIUC-ATREL database

NEW DATA

As part of this project, new tests are being conducted. The database is being updated as they are collected from the test sections. Currently, two sites have performed the tests. Florida DOT and Ohio have conducted tests this winter and data were collected.

The Florida data include pressure and strain measurements at the bottom of the AC layer under various loading and tire configurations. The following table shows the test matrix for Florida's tests.

Table 11. Test matrix for Florida DOT test sections

Tire Type	Inflation Pressure (psi)	Tire Loading (kips)				
		6	8	10	14	18
NGWB and Dual	80	6	8	10	14	18
NGWB and Dual	100	6	8	10	14	18
NGWB and Dual	110	6	8	10	14	18
NGWB and Dual	125	6	8	10	14	18
Dual Only	60/110*	6	8	10	14	18
Dual Only	80/110*	6	8	10	14	18

*Indicates differential tire inflation pressure

A truck test was conducted on the Ohio test sections, and some data were collected. Those sections include two mainline and two ramp sections. The collected data include six heavy-load cases (14 kips-half axle load) out of total of 48 cases considered in the design matrix. The installed sensors consist of various pressure cells, strain gauges, and LVDTs at different depths. In total, 65 measured sensor readings were collected for each case. To obtain the most accurate data, each case was run multiple of times by a truck passing over the section. Also, tire wandering was measured. The raw data were filtered and stored in the database.

Typical Plots

The raw data from the Ohio sections were filtered and stored in the database. The filtering process consists of the following steps: transferring data to the origin, smoothing, finding local optima, plotting, and storing the plots. The following figures show some typical responses.

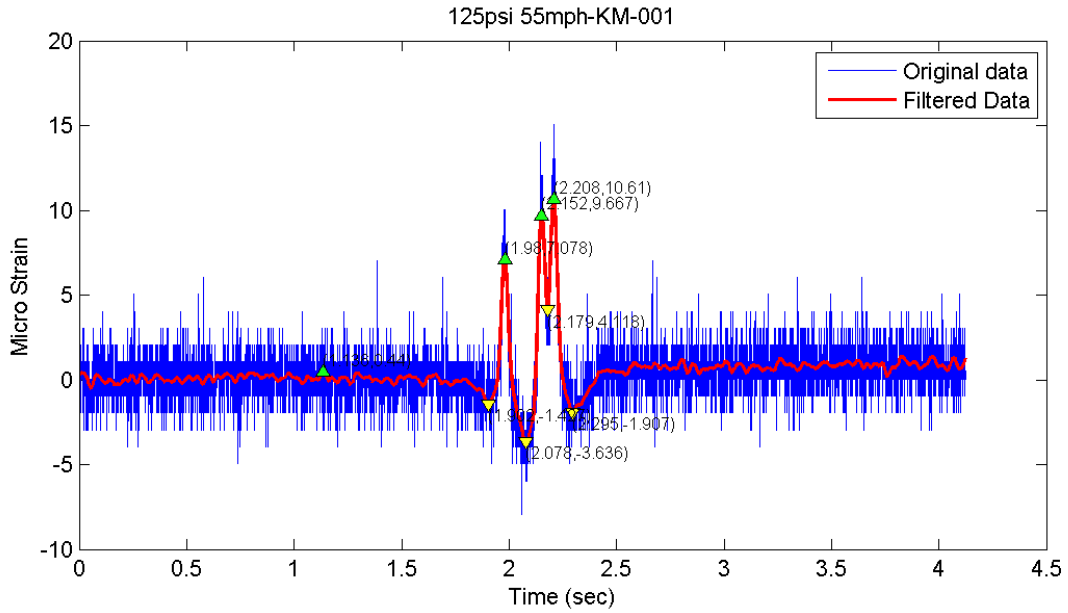


Figure 16. Typical plot for longitudinal strain gage on top of base layer, dual-tandem tire configuration

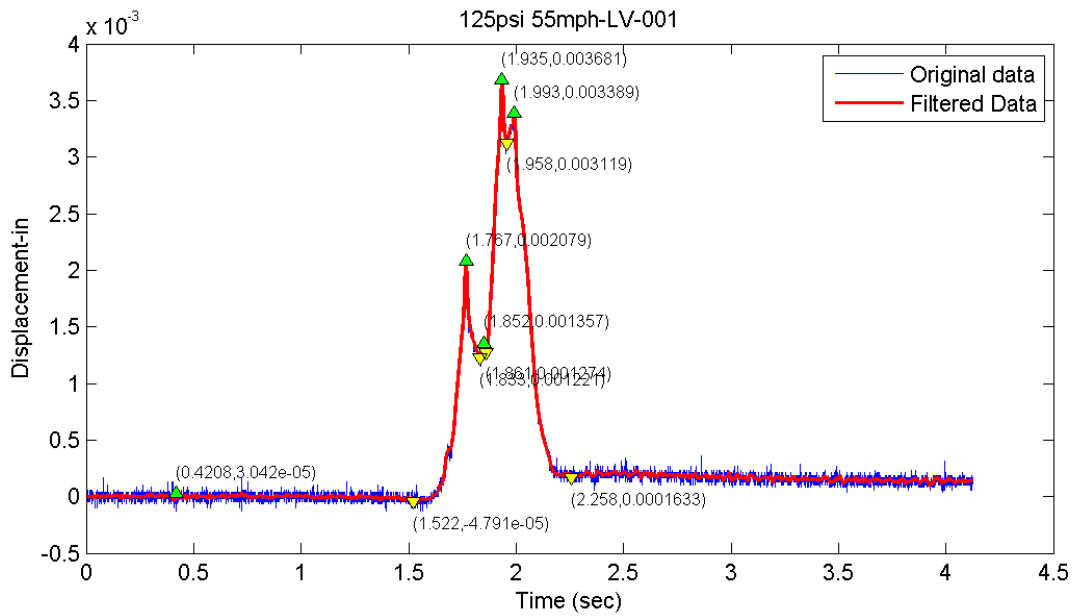


Figure 17. Typical plot for deep LVDT, dual-tandem tire configuration

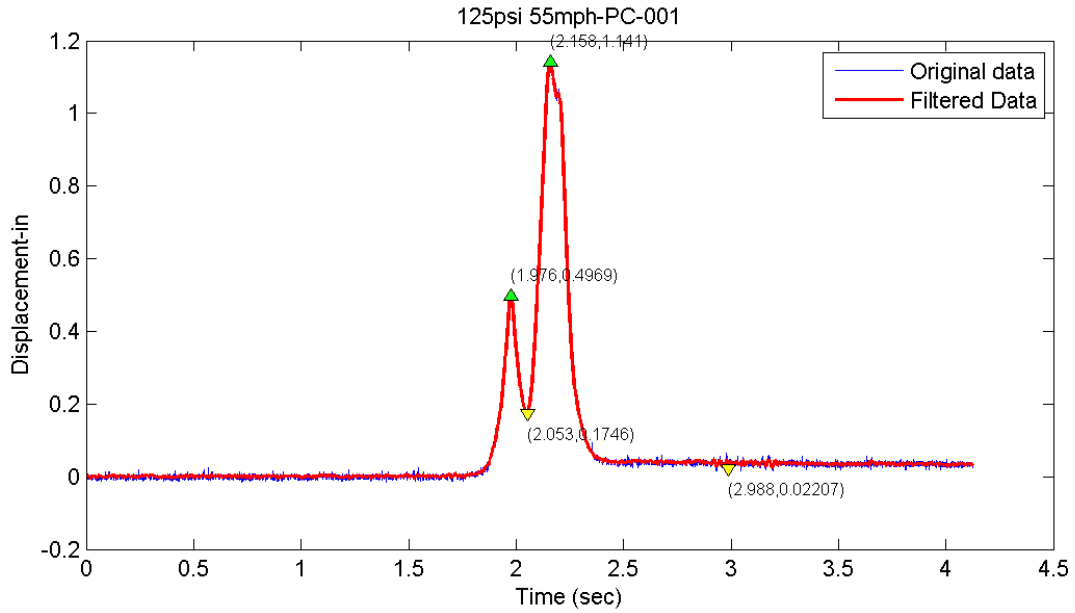


Figure 18. Typical plot for pressure cell on top of the subgrade, dual tire configuration

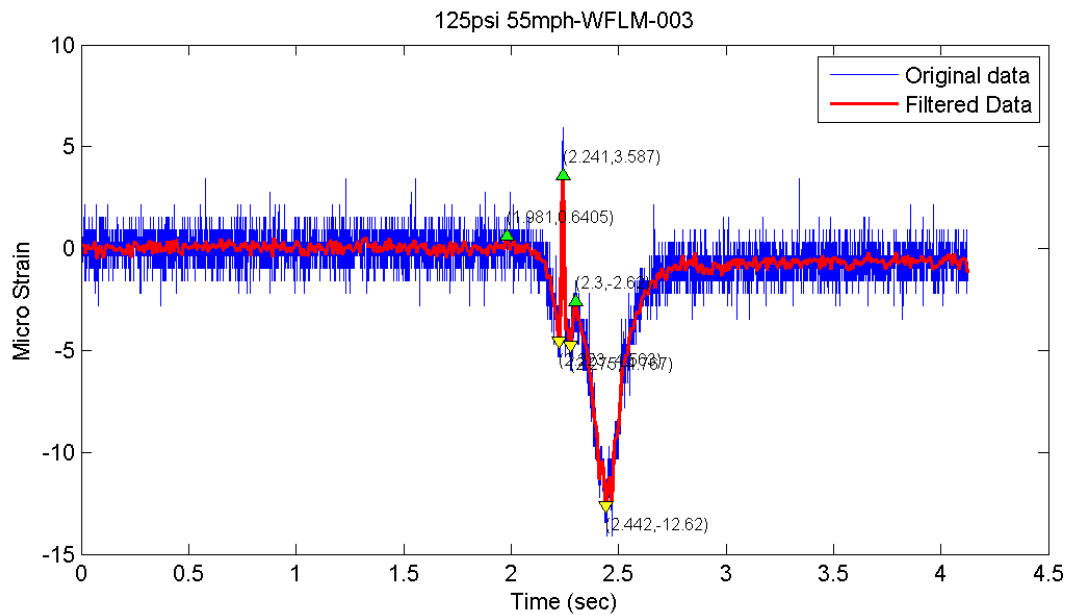


Figure 19. Typical plot for longitudinal component of rosette in square hole, dual-tandem tire configuration

APPENDIX F

OHIO CONSTRUCTION

SITE PREPARATION

In preparation for the site construction and instrumentation of the perpetual pavement sections in Ohio, research engineers and graduate students from ATREL organized a two-week-long sample material acquisition from all the layers of the three sections. The sample material consisted of loose mixtures and Superpave gyratory compacted (SGC) specimens that were estimated for the testing matrix, which would be performed at ATREL and Texas A&M University (TAMU). Ohio University (OU) installed the test site instrumentation.

Three pavement structures were built in Ohio: Sections A and B consisted of 13 in AC and 6 in asphalt treated base (ATB); and Section C consisted of 15 in AC and 8 in of ATB.

INSTRUMENTATION

The detailed scheme of instrument installation is presented in Figure 20 through Figure 25. The instruments consisted of:

- H-type strain gauges installed at three different depths: the bottom of the fatigue resistant layer (FRL), the bottom of the ATB, and the bottom of upper lift of the surface layer.
- Six longitudinal sensors at the bottom of the FRL, as well as six at the bottom of the ATB (three longitudinal and three transverse) and four close to the surface (two longitudinal and two transverse).
- Four pressure cells: two installed on top of the subgrade, and two at the bottom of the FRL.
- A total of 16 SGR were installed in Section A and B, two holes total, eight rosettes in each hole at four different depths. Out of the two holes, one was circular and other was rectangular. The locations of the SGR were at the middle of each lift. Figure 22 shows the detail of the rosette instrumentation.
- In each hole, two rosettes were installed at each depth (four depths total per hole) of Sections A, B, and C (see Figure 22 and Figure 23).

ASPHALT LAYER CONSTRUCTION AND INSTRUMENT INSTALLATION

The scheduled day for building the test path for the FRL and ATB layers was September 12, 2012. The ATREL research engineers visited the AC manufacturing plant prior to the initial day of AC construction to ensure that there would be an appropriate space for the mobile lab setup and to collect dense-graded aggregate base (DGAB) samples. A small oven and four mobile compactors were brought to the plant to accommodate the AC manufacturing pace for the three test sections (Figure 26). The crew members consisted of two research engineers and two graduate students who managed the mobile lab and specimen compaction, and another two graduate students who were on-site to observe and document the location of each haul truck in order to correlate each compacted specimen to its test site location. At the end of the first day, 16 pilot samples were compacted for each of the FRL and ATB layers.

During the next day (September 13, 2012), instruments were installed, including six strain gauges, two thermocouples, and two pressure cells in each of the sections at the bottom of the FRL (Figure 29 and Figure 30). The locations of the instruments were marked, and a tied string was used to ensure that the instruments lay on the same axis. It should be noted that prior to the ATREL crew arrival at the test site, the DGAB was built, and two Geokon pressure cells were installed (Figure 27). For H-type strain gauge installation, a manual sieve was used to obtain finer AC mix, which was used as the leveling material for the instrument. After the strain gauge was set in place, additional finer AC mix was compacted over the strain gauge (Figure 29). The wires connecting the instrumentation to the data acquisition equipment were gathered into a single group, and duct tape was placed over them for protection. The wire ends were put on the side of the road and were checked using a voltage reader.

Another observation during the initial day of AC construction included heaving of the weak DGAB layer at Section B, which could be due to rainfall on the previous weekend and incomplete drying of the layer. This was observed as the paver and haul trucks passed (Figure 31). FRL sampling on this day accumulated to 4,200 lb of loose mixture stored in canvas bags (60 bags containing approximately 70 lb per bag), 60 SGC samples, and 1,400 lb of loose mixtures stored in steel buckets (20 buckets containing approximately 70 lb per bucket).

On September 14, 2012, the ATB layers were built: 6 in and 4 in thick lifts were placed on Section A/B and Section C, respectively (Figure 32). Similar instrument installation techniques were used for the eight strain gauges at the bottom of ATB placed at each section, two of which had a 45° orientation. The following are several observations: (1) the distance between the 45°

sensors is only 1 ft; (2) truck tires passing closely to the line of sensors could cause misalignment; and (3) rutting of the FRL occurred at the same area of the weak DGAB.

On September 15, 2012, the test path for the intermediate layer was constructed, in which 16 pilot specimens were compacted. The AC mixture remained in the silo for approximately five hours. Moreover, due to unsatisfactory results of the intermediate layer test path construction, an additional eight pilot specimens were collected and the crew determined that paving should not be performed. Inclement weather and issues of the asphalt plant led to the halt of the test site construction for three days.

Construction resumed on September 20, 2012, and the intermediate and surface layers were placed. Six strain gauges were installed at the bottom of the intermediate layer; two of the gauges had a 45° orientation (Figure 36). The total amount of the intermediate and surface layer samples gathered consisted of 4,200 lb of loose mixtures stored in canvas bags (60 bags containing approximately 70 lb per bag), 60 SGC samples, and 1,400 lb of loose mixtures stored in steel buckets (20 buckets containing approximately 70 lb per bucket), as shown in Figure 37.

It is noteworthy that although the layers were paved on Thursday (September 20, 2012), the sensors were placed on Wednesday (September 19, 2012). In addition, at Section A, it was observed that the contractor placed an inappropriate ATB thickness relative to the design thickness. Therefore, the area was milled and re-placement of ATB to the appropriate thickness was done (Figure 38). Another observation was the truck tire passing over the line of sensors on Section A, which could influence the alignment and response mechanism of the sensors (Figure 39).

After the final day of the two-week material acquisition and site construction, the mobile laboratory organized by the ATREL crew was removed from the plant site (Figure 40), and all other materials, such as the bagged and compacted samples and the steel buckets that exceeded the space limit of the hauling truck and trailer, were moved to the a storage unit (Figure 40 and Figure 41).

Currently, testing is being conducted at ATREL on the samples/specimens collected from the field. Semi-circle beam and compact disk tests have been completed for all four materials from Ohio. Push-pull and indirect tensile tests are being conducted, and both strength and creep tests are being considered.



Figure 20. Pavement structure and instrumentation of Sections A and B (13-in thick)

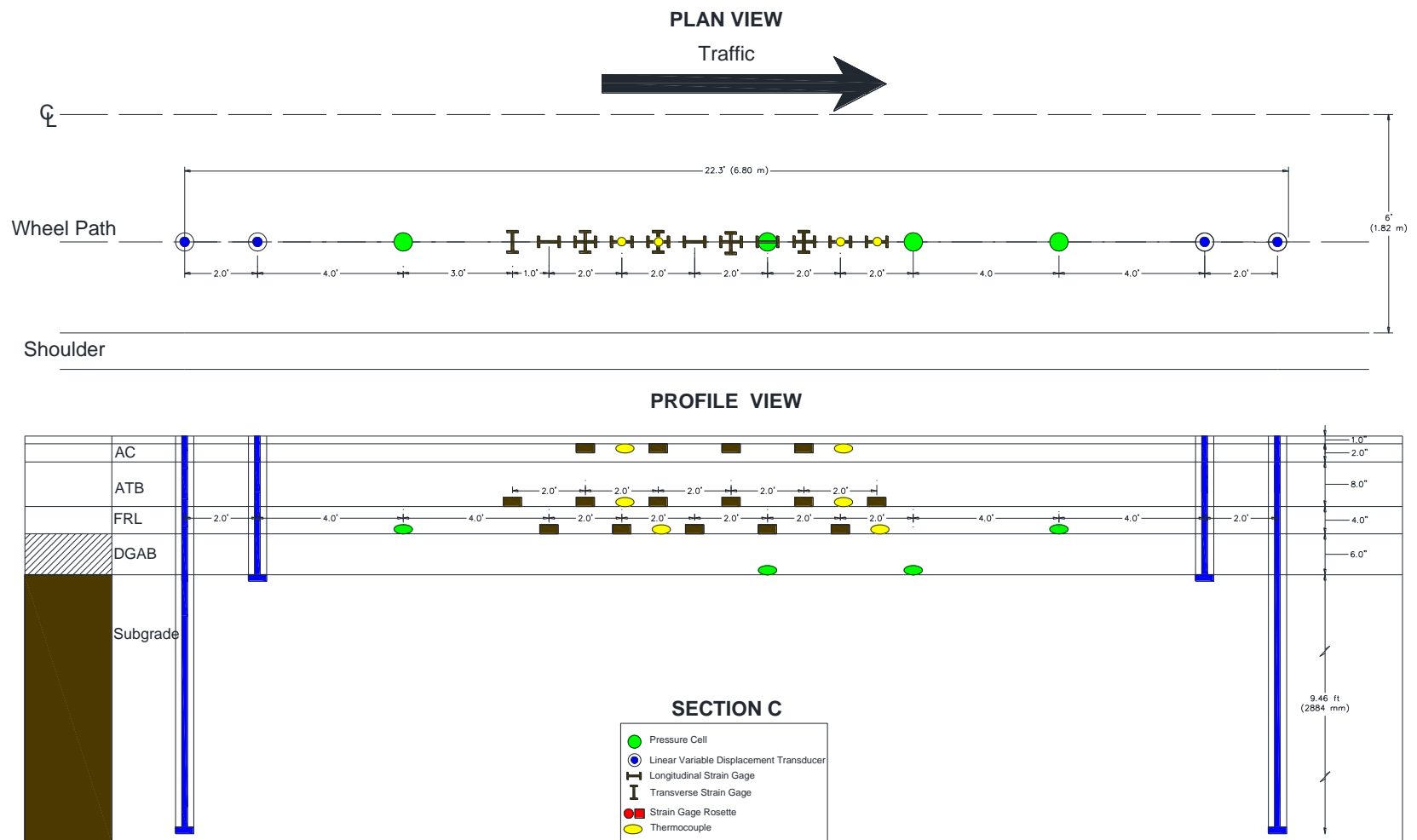


Figure 21. Pavement structure and instrumentation of Section C (15-in thick)

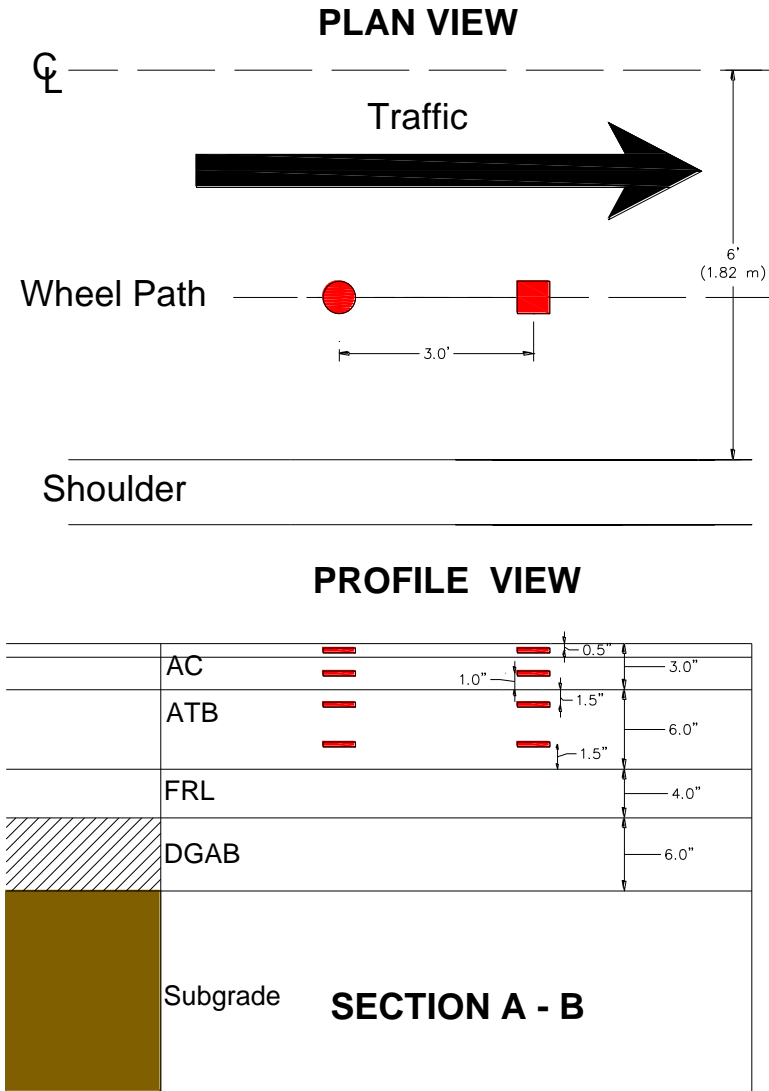


Figure 22. Detail of rosette instrumentation for Sections A and B

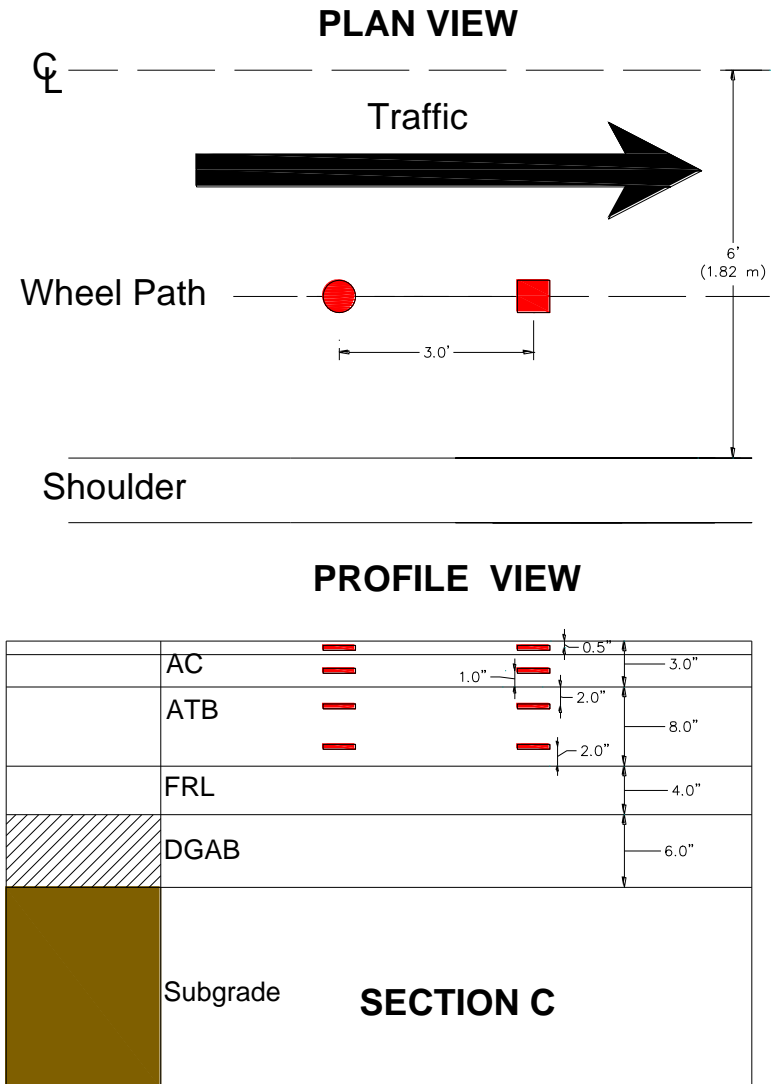


Figure 23. Detail of rosette instrumentation for Section C

CROSS SECTION

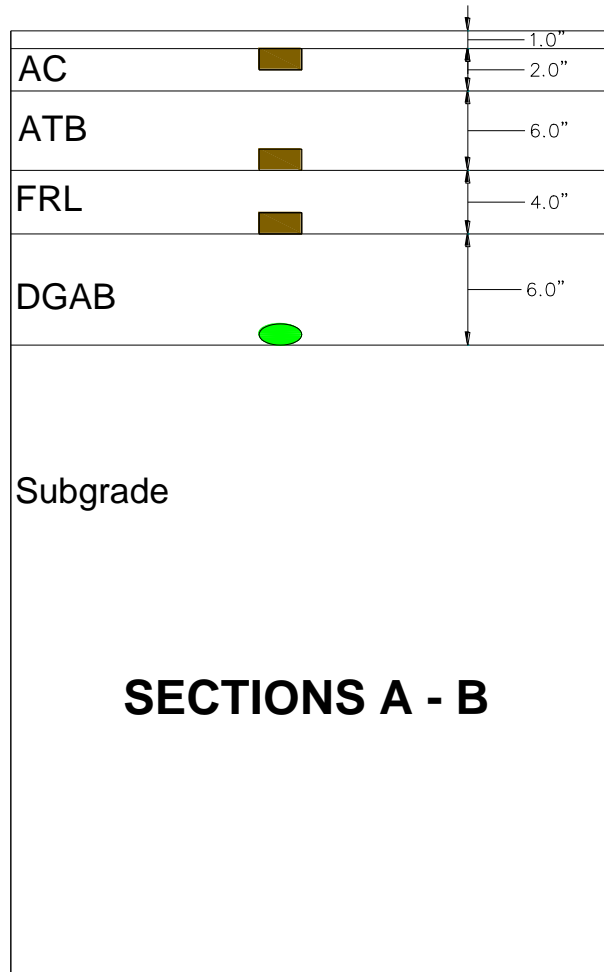


Figure 24. Cross section of pavement structure and instrumentation for Sections A and B

CROSS SECTION

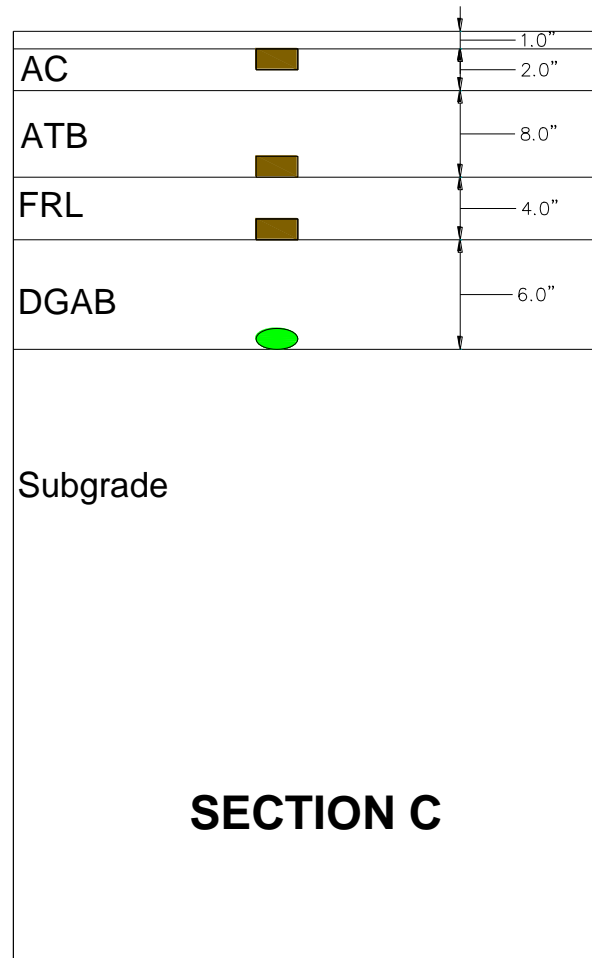


Figure 25. Cross section of pavement structure and instrumentation for Section C



Figure 26. Setup of mobile lab



Figure 27. Geokon pressure cells on top of the subgrade



Figure 28. Instrumentation at the bottom of DGAB in Section A



Figure 29. Installation of sensor at the bottom of the FRL in Section A



Figure 30. Instrumentation at the bottom of FRL in Sections B and C



Figure 31. Weak DGAB in Section B



Figure 32. Instrumentation at the bottom of the ATB



Figure 33. 45° strain gauge 1 ft apart from adjacent sensors



Figure 34. Possible misalignment of sensors after truck passes



Figure 35. Rutting of FRL due to weak DGAB



Figure 36. Instrumentation at the bottom of the intermediate layer



Figure 37. Compacted samples of intermediate and surface layers



Figure 38. Milling and fill of ATB in Section A



Figure 39. Truck ran over sensor in Section A



Figure 40. Mobile laboratory removed from plant

APPENDIX G

FLORIDA PAVEMENT SECTIONS

BACKGROUND

The Federal Highway Administration has sponsored a national study to assess the impact of wide base tires on pavement damage. As part of this study, the Florida Department of Transportation (FDOT) has constructed and instrumented two test sections to measure pavement response. This appendix documents the effort to construct, instrument, and test these sections.

FDOT'S ACCELERATED PAVEMENT TESTING FACILITY

Florida's Accelerated Pavement Testing (APT) facility is housed within the State Materials Research Park in Gainesville. The original test lanes measured 150 feet long and 12 feet wide. A recent expansion of the test track extended each lane an additional 300 feet. The supporting soil layers consist of a 10.5 inch limerock base over a 12 inch mixture of limerock and native A-3 soil. Two additional 50 foot long test tracks (referred to as the test pits) are enclosed by a sump with an interconnecting channel system for controlling the water table. A photograph of the original test tracks and empty test pits are shown in Figure 43.



Figure 43. HVS Test tracks and test pits

Accelerated loading is performed using a Heavy Vehicle Simulator (HVS), Mark IV model. The HVS can apply wheel loads between 7 and 45 kips at speeds of 2 mph to 8 mph along a 30-foot test strip. The effective test segment within this span is approximately 20 feet. The remaining 5 feet, at either end of the test strip, allows the load wheel to reach programmed parameters controlling load and speed levels. Wheel wander of up to 30 inches can be induced. A heater system and insulated panels (shown in Figure 44) maintain a constant testing temperature within the test section area.



Figure 44. Insulated panels on HVS

CONSTRUCTION, INSTRUMENTATION, AND LOADING

TEST SECTION CONSTRUCTION

Two test sections were constructed during October 2012. The first section on the east test pit while the second was constructed on lane 7 of the test track extension. The test pit pavement consisted of two similar 1.5 inch Superpave (SP-12.5) layers with a PG 67-22 asphalt binder. The test track consisted of a 1.5 inch SP-12.5 layer with a PG 67-22 asphalt binder, a 1.5 inch SP-12.5 layer with

a PG 76-22, and a 1.0 inch 4.75 mm mixture with a PG 76-22. The pavement sections were constructed in accordance with FDOT specifications and standards. The pavement structures for these sections are shown in Figure 45.

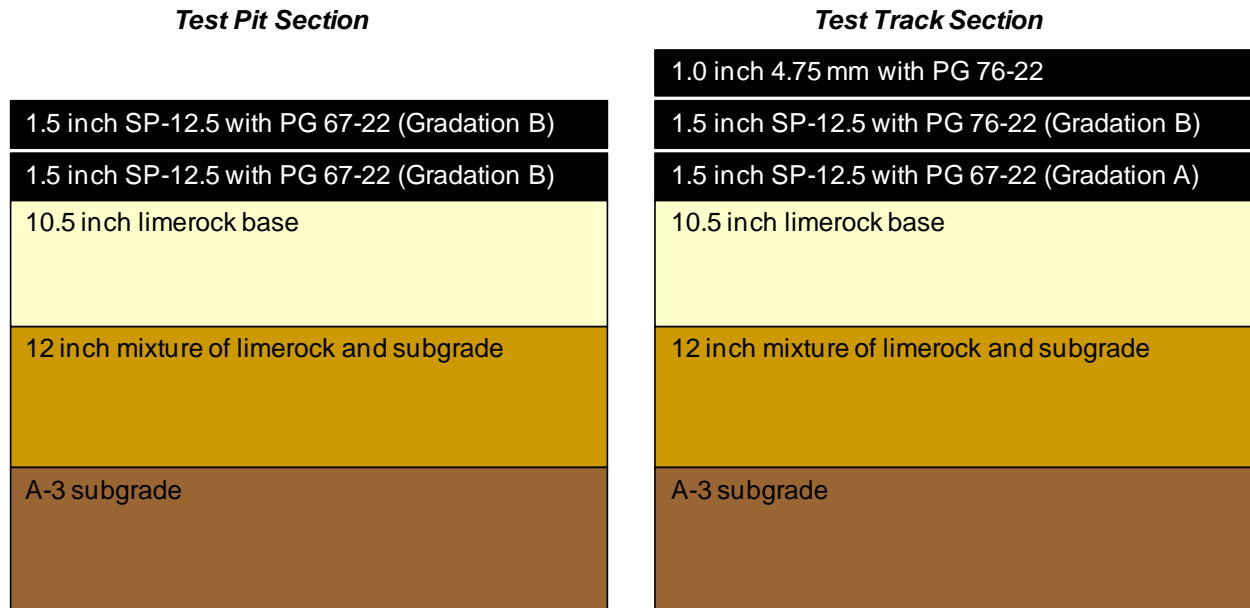


Figure 45. Pavement structure of test sections

INSTRUMENTATION

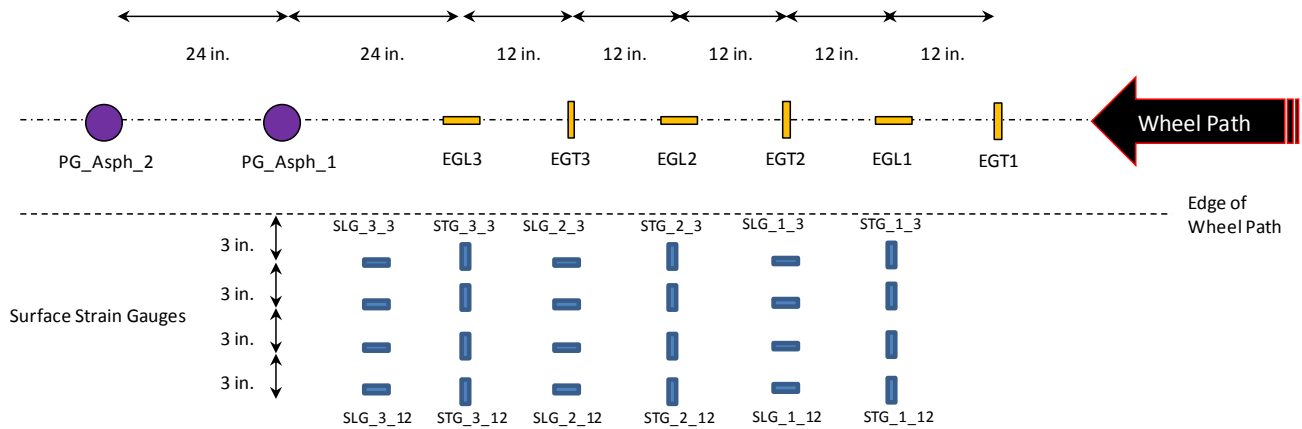
Each test section was instrumented to measure pavement response due to wheel loading. Prior to construction, each embedded sensor was placed in the appropriate location, labeled, and checked for adequate response. Immediately after construction, the response was again checked to make sure each embedded sensor survived the compaction and heat associated with the placement of HMA. Standard sensor installation methods used by FDOT can be found on the State Materials Office website¹. Table 12 summarizes the types of sensors and locations the sensors were placed. Diagrams of the exact sensor locations are shown in Figure 46 and Figure 47. Instrumentation data was collected with a mobile data acquisition (DAQ) system (Figure 48) at 200 Hz for the surface gauges and pressure cells and at 100 Hz for the embedded H-gauges.

¹ <http://www.dot.state.fl.us/statematerialsoffice/pavement/research/apt/documents/instrumentation.pdf>

Table 12. Sensor Types and Locations

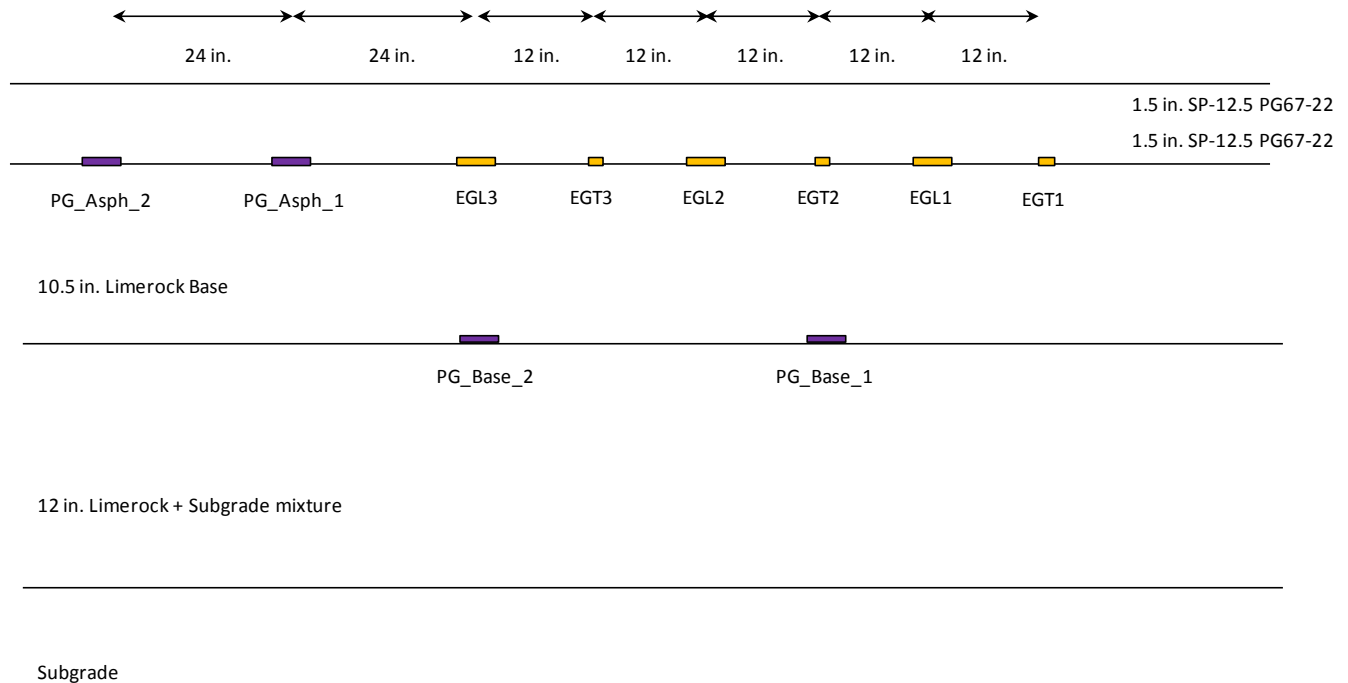
Sensor Type	Number of Sensors per Test Section	Model	Vertical Location	Offset from Wheel Path
Surface strain gauge	24	Tokyo Sokki PFL-30-11-5L	HMA surface	Transverse and longitudinal orientations at various offsets from wheel path edge
Asphalt strain gauge	6	Tokyo Sokki KM-100HAS	Bottom of new HMA	Transverse and longitudinal orientations below tire center
Pressure cell	2	RST Instruments LPTPC09-S	Bottom of new HMA	Below tire center
Pressure cell (Test Pit only)	2	Geokon 3500	Bottom of base	Below tire center

Pressure cells and H-gauges at bottom of asphalt



Note: When the dual tire is inflated with differential pressure, the tire with the lower inflation pressure is nearest the surface strain gauges.

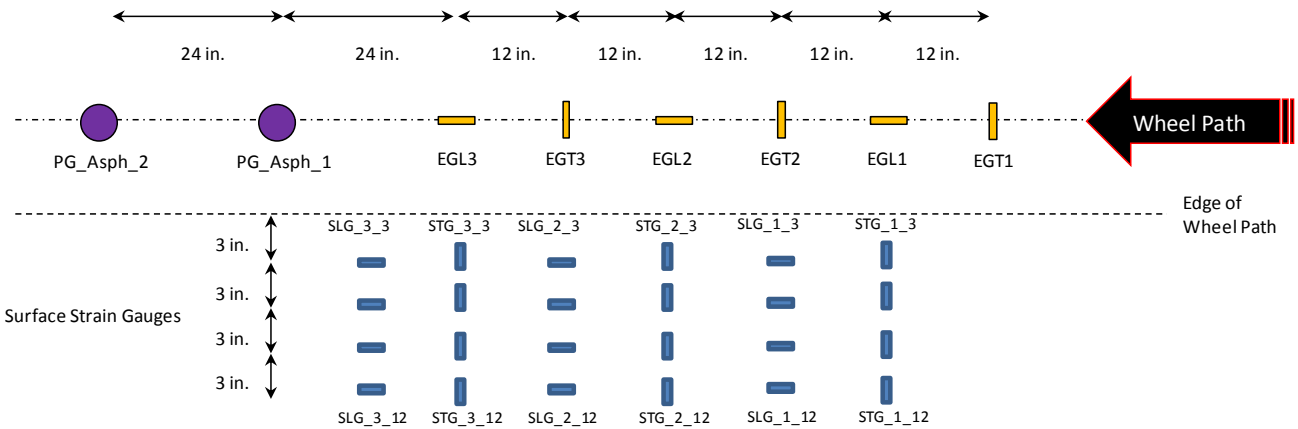
a) Test pit instrumentation plan view



b) Test pit instrumentation elevation view

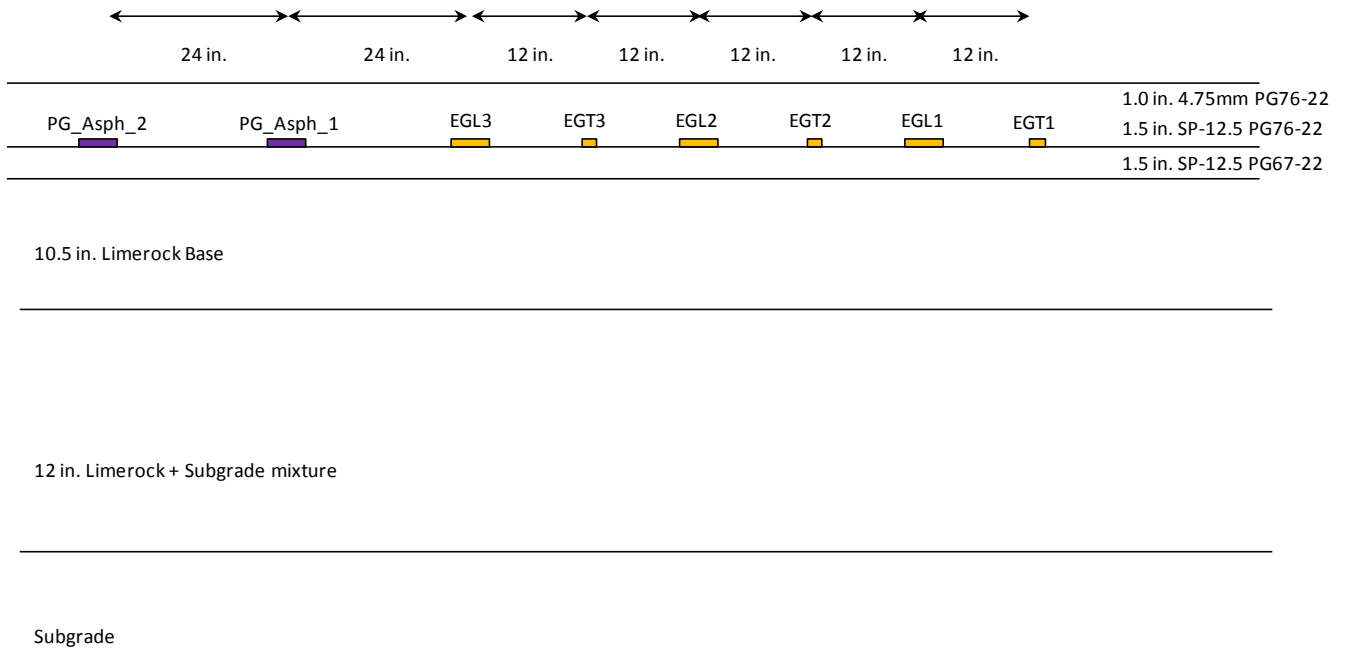
Figure 46. Test pit instrumentation layout

Pressure cells and H-gauges at bottom of asphalt



Note: When the dual tire is inflated with differential pressure, the tire with the lower inflation pressure is nearest the surface strain gauges.

a) Test track instrumentation plan view



b) Test pit instrumentation elevation view

Figure 47. Test track instrumentation elevation view



Figure 48. Mobile DAQ system

MATERIAL SAMPLING

HMA material was sampled from delivery trucks during construction. Table 13 summarizes the laboratory tests that will be conducted using the sampled material. Due to the current laboratory workload, little progress has been made on the test plan. A meeting was held on April 10 with the research laboratory engineer to discuss priorities and schedules. The mixtures used in the tire study have received a higher priority and APT personnel have volunteered to conduct IDT tests as soon as samples have been prepared. Volumetric data (binder content, air voids, etc.) have been determined and are currently being summarized. In addition to testing of sampled material from delivery trucks, 30 cores will be extracted from each test section in the upcoming days. Arrangements will be made for pick-up or shipment of the cores.

Table 13. Laboratory Test Plan

Binder Testing Plan	
PG Binder Testing	In compliance with AASHTO M 320-10 and Section 916 (July 2013)
Multiple Stress Creep Recovery (MSCR) Test	- The environmental grade temperature for the State of Florida (67 °C)
Mixture Testing Plan	
Typical Volumetric Properties	- Sampled from truck (i.e. plant mix)
Superpave IDT at 10 °C	- Samples on plant mixes compacted using the Superpave Gyratory Compactor (SGC) - 4 replicates
Asphalt Mixture Performance Tester (AMPT)	- Samples on plant mixes compacted using the Superpave Gyratory Compactor (SGC) - 3 replicates for dynamic modulus test and 2 replicates for flow number test per test condition
Asphalt Pavement Analyzer (APA)	- Samples on plant mixes compacted using the SGC - 2 replicates per test condition
Confirmation of In-Situ Density and Volumetrics	- Post-construction cores

HVS LOADING

Several combinations of inflation pressure, tire load, and pavement temperature were used for each tire type as shown in Table 14. HVS loading was initiated January 24 on the test pit using the dual tire and was completed on February 12. HVS loading on the test track was initiated on February 20 using the 445 mm wide base tire and was completed on April 10. A main motor failure during loading of the test track delayed testing for more than two weeks.

Table 14. HVS Test Matrix

Tire Type	Inflation Pressure (psi)	Tire Load (kips)				
		6	8	10	14	18
NGWB & Dual	80	6	8	10	14	18
NGWB & Dual	100	6	8	10	14	18
NGWB & Dual	110	6	8	10	14	18
NGWB & Dual	125	6	8	10	14	18
Dual Only	60/110	6	8	10	14	18
Dual Only	60/110	6	8	10	14	18

Each loading combination conducted at 25⁰C, 40⁰C, and 55⁰C

REFERENCES

- Al-Qadi, I.L., Dessouky, S.H., Kwon, J., and Tutumluer, E. (2008). “Geogrid in Flexible Pavements Validated Mechanism.” In Transportation Research Record: Journal of the Transportation Research Board, No. 2045, Transportation Research Board of the National Academies, Washington, D.C., pp. 102-109.
- ASTM D882: Standard Test Method for Tensile Properties of Thin Plastic Sheeting
- ASTM E1640: Standard Test Method for Assignment of the Glass Transition Temperature By Dynamic Mechanical Analysis
- Greene, J., Toros, U., Kim, S., Byron, T., and Choubane, B. (2010). “Impact of Wide-Base Single Tires on Pavement Damage.” In Transportation Research Record: Journal of the Transportation Research Board, No. 2155, Transportation Research Board of the National Academies, Washington, D.C., pp. 82-90.
- Harvey, J., and Popescu, L. (2000). Rutting of Caltrans Asphalt Concrete and Asphalt-Rubber Hot Mix Under Different Wheels, Tires and Temperatures – Accelerated Pavement Testing Evaluation. Report Prepared for California Department of Transportation, Pavement Research Center, Institute of Transportation Studies, University of California, Berkeley.
- Tutumluer, E. (2008). State of the Art: Anisotropic Characterization of Unbound Aggregate Layers In Flexible Pavements. Engineering Mechanics Conference. Minneapolis, MN
- Tutumluer, E. and Thompson, M. (1998). Anisotropic Modeling of Granular Bases. Final Report for the Federal Highway Administration
- Xiao, Y., Tutumluer, E., Siekmeier, J. (2011) Mechanistic–Empirical Evaluation of Aggregate Base and Granular Subbase Quality Affecting Flexible Pavement Performance in Minnesota. *Transportation Research Record*. 2227, 97-106.
- Xue, W., Weaver, E. (2011). “Pavement Shear Strain Response to Dual and Wide-Base Tires.” In Transportation Research Record: Journal of the Transportation Research Board, No. 2225, Transportation Research Board of the National Academies, Washington, D.C., pp. 155-164.